Three-dimensional crack growth with *hp*-generalized finite element and face offsetting methods

J.P. Pereira[†], C.A. Duarte[†], and X. Jiao[‡]

March 10, 2010

[†]*Department of Civil & Environmental Engineering,*
University of Illinois at Urbana-Champaign, 205 North Mathews Ave., Urbana, IL 61801, U.S.A.
[‡]*Department of Applied Mathematics and Statistics, Stony Brook University, Stony Brook, NY 11794-3600, U.S.A.*

Abstract

A coupling between the *hp-version* of the generalized finite element method (*hp*-GFEM) and the face offsetting method (FOM) for crack growth simulations is presented. In the proposed GFEM, adaptive surface meshes composed of triangles are utilized to explicitly represent complex three-dimensional (3-D) crack surfaces. By applying the *hp*-GFEM at each crack growth step, high-order approximations on locally refined meshes are automatically created in complex 3-D domains while preserving the aspect ratio of elements, regardless of crack geometry. The FOM is applied to track the evolution of the crack front in the explicit crack surface representation. The FOM provides geometrically feasible crack front descriptions based on *hp*-GFEM solutions. The coupling of *hp*-GFEM and FOM allows the simulation of arbitrary crack growth with concave crack fronts independent of the volume mesh. Numerical simulations illustrate the robustness and accuracy of the proposed methodology.

Keywords: Generalized finite element method; Extended finite element method; High-order approximations; Face offsetting method; Crack growth.

1 Introduction

In industry, designers often utilize computational simulations of fracture mechanics problems in life prediction of engineering structures. Life prediction of engine components, structural members of aircraft fuselage, riser pipes in offshore platforms and pipeline joints are examples of industrial problems in which three-dimensional (3-D) computational fracture mechanics analysis is broadly applied. In these cases, crack growth assessment is a major requirement, and engineering decisions must be based on accurate evaluation of fracture mechanics quantities such as energy release rate and stress intensity factors [59, 60]. These quantities are, in turn, dependent on the accuracy of the 3-D numerical analysis performed.

The finite element method (FEM) has been broadly used for many decades to perform crack growth analysis of industrial complexity problems [21, 40, 61, 79, 80]. The application of the FEM to this class of problems faces several issues regarding crack surface discretization and excessive computational cost [78]. In the FEM, it is a demanding task to fully automate the generation of meshes in complex 3-D geometries satisfying discontinuities and aspect ratio requirements.

Partition-of-unity methods [5] such as the Generalized FEM (GFEM) [14] and the eXtended FEM (XFEM) [71] are promising techniques to overcome the shortcomings of the standard FEM in crack growth simulations. In these methods, discontinuities in the solution can be represented via suitable enrichment functions coupled with geometrical descriptions of crack surfaces, which are *independent of the volume mesh*. The elements have no requirement to fit the crack surface. This feature of the partition of unity methods greatly facilitates mesh refinement, which can be easily applied in localized regions of the discretization. A survey of 3-D crack growth modeling with partition-of-unity methods is presented in [57].

When applied to three-dimensional fracture mechanics problems, partition of unity methods usually rely on a computational geometry technique to represent the crack surface and the enrichment functions that are utilized to approximate the discontinuous and singular components of the solution. In this paper, the methods used in the geometrical description of the crack surfaces are classified into two groups: implicit and explicit.

Implicit methods use a three-dimensional volume mesh to represent a crack surface. In these methods the fidelity of the crack surface description depends on the refinement of the volume mesh. One example of this type of crack surface representation is the level set method [63]. Belytschko and co-workers coupled the XFEM with level set method for static crack and crack growth simulations [26, 39, 71]. Sukumar et al. [9, 70] have also introduced fast marching techniques to track the evolution of three-dimensional crack surfaces in XFEM simulations. More recently, Duan et al. [12] introduced the element local level set method for 3-D dynamic crack growth analysis with the XFEM. A detailed review of crack surface representation with level set methods in XFEM simulations can be found in [18].

Other examples of implicit crack surface representation are the methods based on a collection of planar cuts or crack planes in tetrahedral elements to represent a crack surface. According to Jäger et al. [28], depending on the crack path tracking strategy, these methods can be subdivided into four categories: fixed, local, non-local and global. The fixed crack tracking strategy is based on standard interface elements, e.g., cohesive elements, and requires the crack path to be known beforehand. In this case, the crack propagates when the interface element, in the predetermined crack path, exceeds a critical failure stress. The local crack tracking scheme can be regarded as a three-dimensional extension of the crack tracking strategy for two-dimensional analysis. In this case, the crack growth is driven by the normal direction of the maximum principal stress and represented by planar cuts in the tetrahedral elements. Each element has its own independent crack plane, which may lead to discontinuities in the overall crack surface representation due to variations of crack plane normals between adjacent elements. In order to prevent these discontinuities, Areias and Belytschko [2] proposed to adjust the planar cut provided by the maximum principal stress according to the intersection points generated by the planar cuts of adjacent elements. In the non-local tracking strategy proposed by Gasser and Holzapfel [23, 24], the crack surface in the neighborhood of the crack front is smoothed out in a least-square sense by a post-processing corrector step. The element crack planes on the neighborhood of the crack front are adjusted in order to provide a smooth crack front for each crack growth step and, consequently, a smooth crack surface representation. The global tracking technique introduced by Oliver et al. [45, 46] applies an auxiliary problem to trace the crack surface path. This tracking technique provides a continuously smooth crack surface by solving an auxiliary heat conduction-like problem within the post-processing phase of the analysis. In this strategy, the crack surface is represented by an isosurface of the solution for the heat conduction-like problem which, in turn, is represented by a collection of planes defined at the element level.

In the studies presented in [2, 12, 28], the overall solution of the problems solved with methods that use implicit crack surface representation is not mesh dependent, as expected. However, the accuracy of the crack surface representation is still mesh dependent since the crack surface is represented by the same

mesh used for the solution of the problem. A remedy for this problem is to incorporate an auxiliary mesh of same spatial dimension as the mesh used in the analysis process to represent the crack [54]. This requires additional bookkeeping and computational cost in order to transfer information between meshes.

Explicit methods for crack surface representation in 3-D use a two-dimensional triangular/quadrilateral mesh embedded in a three-dimensional space to represent the crack surface. By design, this type of representation provides a continuous crack surface with no extra computational cost related to the solution of auxiliary problems. In this case, the crack surface can have an arbitrary shape and no volume mesh refinement is required to improve the accuracy of the crack surface representation. Moreover, special geometrical features of the surface, such as sharp turns, which are very common in mixed-mode simulations, can be easily represented without additional difficulties. The accuracy of crack representation is important for problems in which the physics depend on the shape of the crack surface, e.g. hydraulic fracture, propagation with cohesive models, crack closure, and so forth. This methodology was successfully applied in conjunction with the GFEM in [14, 15, 31, 32, 50, 51] as well as the element-free Galerkin method [33]. More recently, the explicit method was extended to represent interfaces in fluid-structure interaction problems using the XFEM [37].

The *hp-version* of the GFEM (*hp*-GFEM) [50] is a robust method that provides accurate solutions in 3-D crack growth simulations. In the *hp*-GFEM, adaptive surface meshes composed of triangles are utilized to represent complex 3-D crack surfaces. At each crack growth step, this method allows automatic creation of high-order approximations on locally refined volume meshes in complex 3-D domains. It also preserves the aspect ratio of volume elements regardless of crack geometry. There is no requirement on the size of the volume mesh elements to improve the accuracy of the crack surface representation. The size of the elements in the explicit crack surface mesh can be modified without changing the size of the problem described by the volume mesh. Furthermore, special features of the crack surface geometry can be easily represented and preserved through the crack growth simulation.

The face offsetting method (FOM) [29] is a numerical technique which was originally developed to track the evolution of 3-D surfaces of, e.g., burning solid propellants. In this paper, the FOM is adapted to track the evolution of complex 3-D crack fronts. In addition, mesh smoothing and mesh adaptation are also introduced for maintaining the quality and fidelity of the crack surface. Based on the *hp*-GFEM solution, a new crack front position is predicted by the FOM. The FOM provides geometrically feasible crack front descriptions by updating the vertex positions and checking for self-intersections of the crack front edges. The *hp*-GFEM coupled with the FOM allows the simulation of complex crack growth independent of the volume mesh. This work presents numerical simulations that demonstrate the robustness of the proposed methodology.

The remaining parts of this paper are organized as follows. Section 2 presents a brief overview of the *hp*-GFEM and the FOM for three-dimensional fracture mechanics problems. The target problem description and the crack growth model are described in Sections 3 and 4, respectively. Numerical examples to verify and validate the proposed approach are presented in Section 5. Finally, Section 6 discusses the main contributions and concluding remarks of this paper.

2 The hp-GFEM and FOM for crack growth problems

This section presents a brief overview of the *hp*-version of the generalized finite element method (*hp*-GFEM) and the face offsetting method (FOM) for three-dimensional crack growth problems. A detailed discussion on the accuracy, robustness and computational efficiency of the *hp*-GFEM for three-dimensional

static fracture mechanics problem is presented in [50, 51]. A more general and detailed description of the FOM can be found in [29].

2.1 Generalized Finite Element Method

2.1.1 GFEM - a brief overview

The generalized FEM [5, 13, 38, 42, 67] can be regarded as a FEM in which the shape functions are constructed by applying the partition of unity concept [4, 16, 17]. It combines the systematic way of building discretizations from the standard FEM and the approximation function flexibility enjoyed by meshfree methods [3, 6, 27, 35, 36]. In the GFEM considered here, a shape function $\phi_{\alpha i}$ is built from the product of a finite element Lagrangian shape function, φ_α, and an enrichment function, $L_{\alpha i}$,

$$\phi_{\alpha i}(\boldsymbol{x}) = \varphi_\alpha(\boldsymbol{x}) L_{\alpha i}(\boldsymbol{x}) \qquad \text{(no summation on } \alpha) \tag{1}$$

where α is the index of a node in the finite element mesh. Figure 1(a) illustrates the construction of GFEM shape functions.

The linear finite element shape functions $\varphi_\alpha,\ \alpha = 1,\ldots,N$, in a finite element mesh with N nodes constitute a partition of unity, i.e., $\sum_{\alpha=1}^{N} \varphi_\alpha(\boldsymbol{x}) = 1$ for all $\boldsymbol{x}$ in a domain Ω discretized by the finite element mesh. This is a key property used in partition of unity methods. Linear combinations of the GFEM shape functions $\phi_{\alpha i}(\boldsymbol{x}),\ \alpha = 1,\ldots,N$ can represent *exactly* any enrichment function $L_{\alpha i}$.

Several enrichment functions can be hierarchically added to any node α in a finite element mesh. Thus, if D_L is the number of enrichment functions at node α, the GFEM approximation, $\boldsymbol{u}^{hp}$, of a function $\boldsymbol{u}$ can be written as

$$\begin{aligned} \boldsymbol{u}^{hp}(\boldsymbol{x}) &= \sum_{\alpha=1}^{N} \sum_{i=1}^{D_L} \underline{\boldsymbol{u}}_{\alpha i} \phi_{\alpha i}(\boldsymbol{x}) = \sum_{\alpha=1}^{N} \sum_{i=1}^{D_L} \underline{\boldsymbol{u}}_{\alpha i} \varphi_\alpha(\boldsymbol{x}) L_{\alpha i}(\boldsymbol{x}) \\ &= \sum_{\alpha=1}^{N} \varphi_\alpha(\boldsymbol{x}) \sum_{i=1}^{D_L} \underline{\boldsymbol{u}}_{\alpha i} L_{\alpha i}(\boldsymbol{x}) = \sum_{\alpha=1}^{N} \varphi_\alpha(\boldsymbol{x}) \boldsymbol{u}_\alpha^{hp}(\boldsymbol{x}) \end{aligned} \tag{2}$$

where $\underline{\boldsymbol{u}}_{\alpha i},\ \alpha = 1,\ldots,N,\ i = 1,\ldots,D_L$, are nodal degrees of freedom and $\boldsymbol{u}_\alpha^{hp}(\boldsymbol{x})$ is a local approximation of $\boldsymbol{u}$ defined on $\omega_\alpha = \{\boldsymbol{x} \in \Omega : \varphi_\alpha(\boldsymbol{x}) \neq 0\}$, the support of the partition of unity function φ_α. In the case of a finite element partition of unity, the support ω_α (often called cloud) is given by the union of the finite elements sharing a vertex node $\boldsymbol{x}_\alpha$ [13]. The equation above shows that the global approximation $\boldsymbol{u}^{hp}(\boldsymbol{x})$ is built by pasting together local approximations $\boldsymbol{u}_\alpha^{hp}, \alpha = 1,\ldots,N$, using a partition of unity. This is a concept common to all partition of unity methods.

2.1.2 *hp*-GFEM for fracture mechanics problems

The local approximations $\boldsymbol{u}_\alpha^{hp},\ \alpha = 1,\ldots,N$, belong to local spaces $\chi_\alpha(\omega_\alpha) = \text{span}\{L_{i\alpha}\}_{i=1}^{D_L}$ defined on the supports $\omega_\alpha,\ \alpha = 1,\ldots,N$. The selection of the enrichment or basis functions for a particular local space $\chi_\alpha(\omega_\alpha)$ depends on the local behavior of the function $\boldsymbol{u}$ over the cloud ω_α. In the case of fracture mechanics problems, the elasticity solution $\boldsymbol{u}$ may be written as

$$\boldsymbol{u} = \hat{\boldsymbol{u}} + \tilde{\tilde{\boldsymbol{u}}} + \breve{\boldsymbol{u}} \tag{3}$$

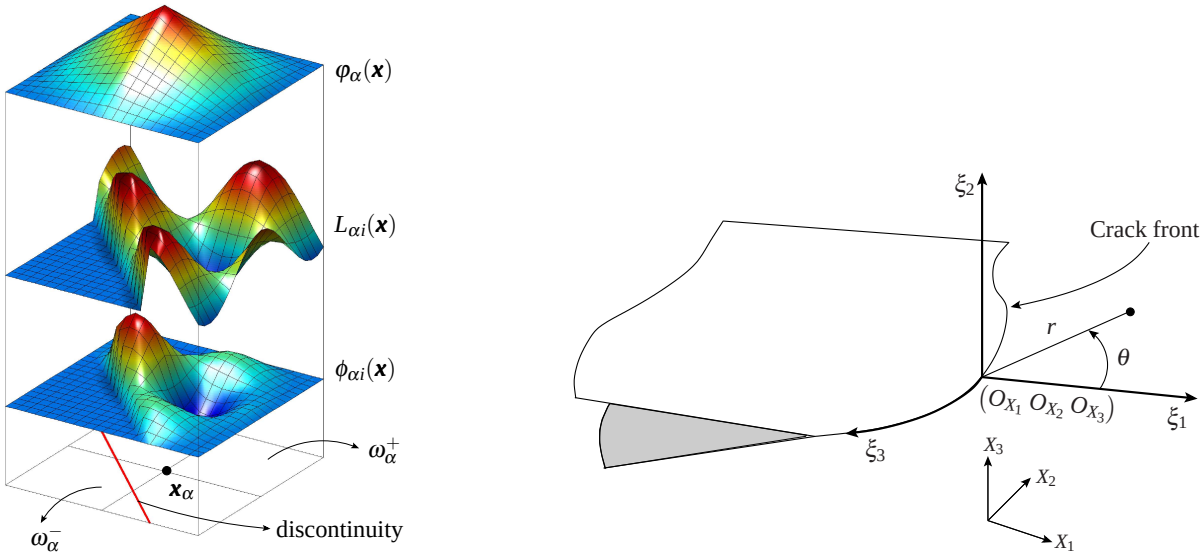

(a) GFEM shape function. (b) Crack front coordinate system.

Figure 1: *Construction process for GFEM shape functions and crack front coordinate system.*

where $\hat{\boldsymbol{u}}$ is a continuous function, $\tilde{\tilde{\boldsymbol{u}}}$ is a discontinuous function but non-singular and $\breve{\boldsymbol{u}}$ is a discontinuous and singular function. This *a priori* knowledge about the solution $\boldsymbol{u}$ is used below to select basis functions for a local space $\chi_\alpha(\omega_\alpha)$.

The selection of enrichment functions is based on the position of the cloud ω_α with respect to the crack surface. The local approximation can be subdivided into three distinct sets:

Local high-order approximation for continuous functions Let $\mathscr{I}_c$ denote a set with the indices of clouds ω_α that do not intersect either the crack surface or the crack front. In this case, a local approximation, $\hat{\boldsymbol{u}}_\alpha^{hp}(\boldsymbol{x})$, of $\boldsymbol{u}$ over ω_α can be written as

$$\hat{\boldsymbol{u}}_\alpha^{hp}(\boldsymbol{x}) = \sum_{i=1}^{\hat{D}_L} \underline{\hat{\boldsymbol{u}}}_{\alpha i} \hat{L}_{\alpha i}(\boldsymbol{x}) \tag{4}$$

where $\hat{D}_L$ is the dimension of a set of polynomial enrichment functions of degree less than or equal to $p-1$. Our implementation follows [13, 42] and the set $\{\hat{L}_{\alpha i}\}_{i=1}^{\hat{D}_L}$ for a cloud associated with node $\boldsymbol{x}_\alpha = (X_{1_\alpha}, X_{2_\alpha}, X_{3_\alpha})$ is given by

$$\{\hat{L}_{\alpha i}\}_{i=1}^{\hat{D}_L} = \left\{1, \frac{(X_1 - X_{1_\alpha})}{h_\alpha}, \frac{(X_2 - X_{2_\alpha})}{h_\alpha}, \frac{(X_3 - X_{3_\alpha})}{h_\alpha}, \frac{(X_1 - X_{1_\alpha})^2}{h_\alpha^2}, \frac{(X_2 - X_{2_\alpha})^2}{h_\alpha^2}, \ldots\right\} \tag{5}$$

with h_α being a scaling factor [13, 42]. These enrichment functions are identical to those defined in [13]. The corresponding generalized FE shape functions, $\hat{\phi}_{\alpha i}$, at a node $\boldsymbol{x}_\alpha$, are polynomials of degree p given by

$$\hat{\phi}_{\alpha i}(\boldsymbol{x}) = \varphi_\alpha(\boldsymbol{x}) \hat{L}_{\alpha i}(\boldsymbol{x}) \qquad i = 1, \ldots, \hat{D}_L \quad \text{(no summation on } \alpha) \tag{6}$$

Local high-order approximation for discontinuous functions Let $\mathscr{I}_{\text{c-f}}$ denote a set with the indices of clouds ω_α that intersect the crack surface but not the crack front. In this case, the solution $\boldsymbol{u}$ over ω_α has continuous and discontinuous non-singular parts. A local approximation, $\boldsymbol{u}_\alpha^{hp}(\boldsymbol{x})$, of $\boldsymbol{u}$ over $\omega_\alpha,\ \alpha \in \mathscr{I}_{\text{c-f}}$, can be written as

$$\boldsymbol{u}_\alpha^{hp}(\boldsymbol{x}) = \hat{\boldsymbol{u}}_\alpha^{hp}(\boldsymbol{x}) + \mathscr{H}\tilde{\boldsymbol{u}}_\alpha^{hp}(\boldsymbol{x}) = \sum_{i=1}^{\hat{D}_L} \underline{\hat{\boldsymbol{u}}}_{\alpha i}\hat{L}_{\alpha i}(\boldsymbol{x}) + \sum_{i=1}^{\tilde{D}_L} \underline{\tilde{\boldsymbol{u}}}_{\alpha i}\mathscr{H}\hat{L}_{\alpha i}(\boldsymbol{x}) \tag{7}$$

where $\mathscr{H}(\boldsymbol{x})$ denotes a discontinuous function defined by

$$\mathscr{H}(\boldsymbol{x}) = \begin{cases} 1 & \text{if } \boldsymbol{x} \in \omega_\alpha^+ \\ 0 & \text{otherwise} \end{cases} \tag{8}$$

ω_α^+ is the part of the cloud ω_α located above the discontinuity (cf. Figure 1(a)). $\hat{\boldsymbol{u}}_\alpha^{hp}(\boldsymbol{x})$ and $\tilde{\boldsymbol{u}}_\alpha^{hp}(\boldsymbol{x})$ are local approximations of $\hat{\boldsymbol{u}}$ and $\tilde{\boldsymbol{u}}$, respectively, and $\hat{L}_{\alpha i}$ is a polynomial enrichment function of degree less than or equal to $p-1$ as previously defined.

The analysis of through-the-thickness cracks presented in [15] shows that the continuous and discontinuous components of the solution $\boldsymbol{u}$ should be approximated using the same polynomial order. Thus, we take $\tilde{D}_L = \hat{D}_L$ in all computations presented in Section 5.

Based on the above, the generalized FE shape functions of degree less than or equal to p used at a node $\boldsymbol{x}_\alpha,\ \alpha \in \mathscr{I}_{\text{c-f}}$, are given by

$$\boldsymbol{\Phi}_\alpha^p = \left\{\hat{\phi}_{\alpha i},\ \tilde{\phi}_{\alpha i}\right\}_{i=1}^{\hat{D}_L} \tag{9}$$

where $\tilde{\phi}_{\alpha i} = \mathscr{H}\hat{\phi}_{\alpha i}$ and $\hat{\phi}_{\alpha i}$ is defined in (6). The enrichment functions $\mathscr{H}\hat{L}_{\alpha i}(\boldsymbol{x}),\ i = 1,\ldots,\hat{D}_L$, are called high-order step functions [15, 50].

Crack front enrichment functions Let $\mathscr{I}_{\text{front}}$ denote a set with the indices of clouds ω_α that intersect the crack front. In this case, terms from the asymptotic expansion of the elasticity solution near crack fronts are good choices for enrichment functions. Two dimensional expansions of the elasticity solution are commonly used as enrichment functions for three-dimensional cracks in finite size domains [13, 14, 39, 71]. As a consequence, a sufficiently fine mesh must be used around the crack front in order to represent the three-dimensional solution effect and achieve acceptable accuracy. A local approximation, $\check{\boldsymbol{u}}_\alpha^{hp}(\boldsymbol{x})$, of $\boldsymbol{u}$ over ω_α, $\alpha \in \mathscr{I}_{\text{front}}$, is defined as

$$\check{\boldsymbol{u}}_\alpha^{hp} = \sum_{i=1}^{2} \begin{bmatrix} \underline{\check{u}}_{\alpha i}^{\xi_1}\check{L}_{\alpha i}^{\xi_1}(r,\theta) \\ \underline{\check{u}}_{\alpha i}^{\xi_2}\check{L}_{\alpha i}^{\xi_2}(r,\theta) \\ \underline{\check{u}}_{\alpha i}^{\xi_3}\check{L}_{\alpha i}^{\xi_3}(r,\theta) \end{bmatrix} \tag{10}$$

where ξ_1, ξ_2 and ξ_3 are directions in a curvilinear coordinate system defined along the crack front, and r, θ and ξ_3 are curvilinear cylindrical coordinates, as illustrated in Figure 1(b). $\underline{\check{u}}_{\alpha i}^{\xi_1}$, $\underline{\check{u}}_{\alpha i}^{\xi_2}$ and $\underline{\check{u}}_{\alpha i}^{\xi_3}$ are degrees of freedom in the ξ_1-, ξ_2- and ξ_3- directions, respectively. Here, the degrees of freedom are scalar quantities, in contrast with those used in the previous local approximations.

The enrichment functions used to approximate displacement fields in the ξ_1, ξ_2 and ξ_3 directions are

given by [13, 14, 41, 43, 50]

$$
\begin{aligned}
\check{L}^{\xi_1}_{\alpha 1}(r,\theta) &= \sqrt{r}\left[(\kappa-\frac{1}{2})\cos\frac{\theta}{2}-\frac{1}{2}\cos\frac{3\theta}{2}\right] \\
\check{L}^{\xi_2}_{\alpha 1}(r,\theta) &= \sqrt{r}\left[(\kappa+\frac{1}{2})\sin\frac{\theta}{2}-\frac{1}{2}\sin\frac{3\theta}{2}\right] \\
\check{L}^{\xi_3}_{\alpha 1}(r,\theta) &= \sqrt{r}\sin\frac{\theta}{2} \\
\check{L}^{\xi_1}_{\alpha 2}(r,\theta) &= \sqrt{r}\left[(\kappa+\frac{3}{2})\sin\frac{\theta}{2}+\frac{1}{2}\sin\frac{3\theta}{2}\right] \\
\check{L}^{\xi_2}_{\alpha 2}(r,\theta) &= \sqrt{r}\left[(\kappa-\frac{3}{2})\cos\frac{\theta}{2}+\frac{1}{2}\cos\frac{3\theta}{2}\right] \\
\check{L}^{\xi_3}_{\alpha 2}(r,\theta) &= \sqrt{r}\sin\frac{3\theta}{2}
\end{aligned}
\tag{11}
$$

where the material constant $\kappa = 3-4\nu$ and ν is Poisson's ratio. This assumes plane strain conditions, which is in general a good approximation far from crack front ends. The above enrichment functions correspond to the first term of the modes *I* and *II*, and to the first and second terms of the mode *III* components of the asymptotic expansion of elasticity solution around a straight crack front, far from the vertices and for a traction-free flat crack surface [72]. More details about the geometrical approximation of the crack front as well as the definition of the crack front coordinate system can be found in [51].

Generalized FEM shape functions built with the enrichment functions (11) must be integrated with care. In the numerical examples presented in this work, this is achieved by using strongly graded meshes at the crack front and an appropriate number of integration points. A detailed study of numerical integration and computational performance of these functions is presented in [48].

Partition of unity shape functions are linear dependent when, for example, both the partition of unity and the enrichment functions span polynomials [13, 66, 75]. This is the case of the GFEM shape functions defined in (6). Algorithms to deal with these linear dependences are described in [13] and an approach to avoid them is proposed in [76]. In this paper, the linear dependencies of the global system of equations are handled using the algorithm presented in [13].

Localized *h*-refinement Analytical enrichment functions, such as (11), are not able to deliver accurate solutions on coarse three-dimensional meshes when the crack front has a complex geometry. Localized mesh refinement must be applied in order to overcome this limitation [19, 50, 51]. Although these analytical enrichment functions require localized mesh refinement, the size of the elements along the crack front in typical *hp*-GFEM meshes is usually one order of magnitude larger than the size of the crack front elements in standard FEM meshes [51]. A detailed convergence analysis on the *hp*-GFEM applied to fracture mechanics problems and on enrichment functions for curved crack fronts with localized *h*-refinement can be found in [50] and [51], respectively.

Localized refinement and unrefinement can be easily applied in crack growth simulations with the GFEM. In the GFEM models for fracture mechanics, the elements in the volume mesh need not fit the crack surface and the crack surface representation is independent of the volume mesh. Numerical examples in Section 5 illustrate this feature of the method.

Crack surface representation In the *hp*-GFEM adopted in this paper, the crack surface is represented by flat triangles with straight edges [50] as illustrated in Figures 6 and 19. Thus, curved crack fronts are approximated by straight line segments. The fidelity of this approximation can be controlled by simply using a finer triangulation of the crack surface. This process is *independent* of the GFEM mesh and does not change the problem size [50]. The explicit crack surface representation provides geometrical information for the construction of crack front coordinate systems and crack front enrichment functions, such as (11). The computational geometry aspects of this construction are presented in detail in [51].

This work extends the formulation of the face offsetting method (FOM), introduced in [29], to track the evolution of the crack front in crack growth simulations. The next section presents a brief introduction of the method and the main FOM techniques applied to crack front evolution.

2.2 The face offsetting method for crack growth

2.2.1 FOM - a brief overview

The face offsetting method (FOM) [29] is a numerical technique used to track the evolution of explicit surfaces. It is an alternative to the level set method [63] that has been broadly used in the extended finite element method context [26, 54, 68]. Given the current position of a surface Γ and either a velocity field $\boldsymbol{v}(\boldsymbol{x},t) : \Gamma \times \mathbb{R} \rightarrow \mathbb{R}^3$ or a normal speed $f(\boldsymbol{x},t) : \Gamma \times \mathbb{R} \rightarrow \mathbb{R}$, the FOM determines the new position of a moving surface at time $t + \Delta t$ by integrating the Lagrangian equations $\frac{d\boldsymbol{x}}{dt} = \boldsymbol{v}(\boldsymbol{x},t)$ or $\frac{d\boldsymbol{x}}{dt} = f(\boldsymbol{x},t)\boldsymbol{n}(\boldsymbol{x},t)$, where $\boldsymbol{n}$ denotes the unit normal to the surface. The FOM solves these equations using a geometric construction based on the Generalized Huygens' or shell-of-influence principle for moving interfaces [29]. It first propagates the faces using a standard time integration technique. At each vertex v, let $\boldsymbol{n}_i$ denote the normal to the ith face incident on v after time integration, and $\boldsymbol{M} = \sum_i \boldsymbol{n}_i \boldsymbol{n}_i^T$ denote the "normal covariance matrix" at v. FOM determines the new position of v by performing an eigenvalue analysis of $\boldsymbol{M}$ and then solving the normal and tangential motions simultaneously. During surface evolution, the FOM also redistributes the vertices to maintain or improve the quality of the surface mesh. It also checks for self-intersection to avoid misrepresentation of the evolving surface. Compared to the level set method, FOM has the advantages of being able to capture sharp turns in surfaces and to be generalized to non-manifold surfaces (such as in branching cracks). More details about these techniques can be found in [29].

In our crack-growth simulations, the crack surface evolution is represented by a sequence of crack front steps using explicit crack surface representation presented in [50, 51]. The crack front vertices, edges, and their incident faces are the only parts of the surface that control its evolution throughout the simulation. In this paper, we adapt the face offsetting method (FOM) to track the evolution of these crack fronts. Two key features of the original FOM method are utilized and adapted here: 1) the prediction of self-intersection and adaptation of time step, and 2) the smoothing and adaptation of the surface mesh along the tangential direction. We hereafter describe these two aspects in more detail.

2.2.2 Crack advance limit

FOM checks the crack front for self-intersection at each step of the crack growth simulation and provides geometrically feasible crack front and crack surface descriptions. For the purpose of detecting self-intersections, consider each vertex on the crack front v_j moving along a straight line from its current position $\boldsymbol{p}_j$ with advance vector $\boldsymbol{d}_j$, which is based on the solution computed by the *hp*-GFEM method presented in Section 2.1.2 and the crack growth criterion presented in Section 4. The line segment can be parameterized

by $\boldsymbol{q}_j = \boldsymbol{p}_j + \beta \boldsymbol{d}_j, 0 \leq \beta \leq 1$. As illustrated in Figure 2, consider a triangle $\boldsymbol{p}_1\boldsymbol{p}_2\boldsymbol{p}_3$ incident on a vertex on the crack front. We refer to such a triangle as a *crack front face*. Let $\boldsymbol{q}_j = \boldsymbol{p}_j + \beta \boldsymbol{d}_j, 1 \leq j \leq 3$ denote these three vertices with a partial increment of $\beta \boldsymbol{d}_j$, where $\boldsymbol{d}_j = \boldsymbol{0}$ for the vertices not on the crack front. The condition to prevent self-intersection of the crack front can be then regarded as the limit of the crack increment $\beta \boldsymbol{d}_i$ that avoids the reversal of the orientation of the crack front faces and of the crack front curve. It therefore suffices to determine a β that prevents such reversals.

We first consider the orientation of the crack front faces. Let $\boldsymbol{q}_{i-j}$ denote $\boldsymbol{q}_i - \boldsymbol{q}_j$ (and similarly for $\boldsymbol{p}_{i-j}$ and $\boldsymbol{d}_{i-j}$). The normal to the triangle $\boldsymbol{q}_1\boldsymbol{q}_2\boldsymbol{q}_3$ with the partial displacements $\beta \boldsymbol{d}_j$ is then

$$\begin{aligned} \boldsymbol{q}_{2-1} \times \boldsymbol{q}_{3-1} &= (\boldsymbol{p}_{2-1} + \beta \boldsymbol{d}_{2-1}) \times (\boldsymbol{p}_{3-1} + \beta \boldsymbol{d}_{3-1}) \\ &= \beta^2 (\boldsymbol{d}_{2-1} \times \boldsymbol{d}_{3-1}) + \beta (\boldsymbol{d}_{2-1} \times \boldsymbol{p}_{3-1} + \boldsymbol{p}_{2-1} \times \boldsymbol{d}_{3-1}) + \boldsymbol{p}_{2-1} \times \boldsymbol{p}_{3-1} \\ &= \beta^2 \boldsymbol{c}_2 + \beta \boldsymbol{c}_1 + \boldsymbol{c}_0, \end{aligned} \tag{12}$$

where $\boldsymbol{c}_0$ is the normal to the crack front face when $\beta = 0$. The orientation of the crack-front face cannot be flipped if β is between 0 and the smaller positive solution to the quadratic equation

$$\boldsymbol{c}_0^T \left(\beta^2 \boldsymbol{c}_2 + \beta \boldsymbol{c}_1 + \boldsymbol{c}_0 \right) = 0. \tag{13}$$

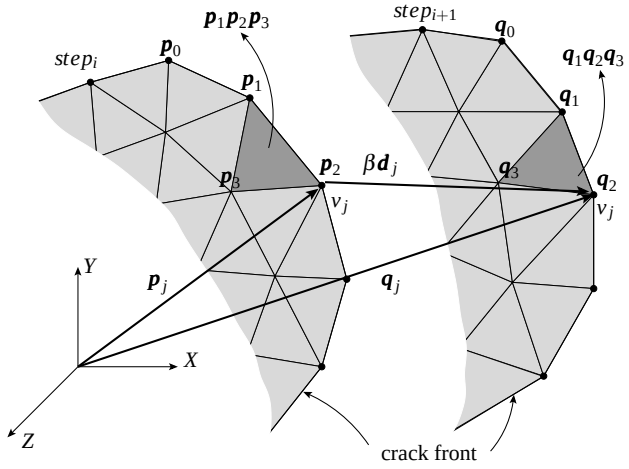

Figure 2: *Illustration of crack advance limit formulation. The triangles on the right denote triangles with partial displacement increments.*

To check the orientation of the crack front curve, consider two consecutive crack front edges $\boldsymbol{p}_0\boldsymbol{p}_1$ and $\boldsymbol{p}_1\boldsymbol{p}_2$, and let $\boldsymbol{q}_j = \boldsymbol{p}_j + \beta \boldsymbol{d}_j, 0 \leq j \leq 2$. Let $\boldsymbol{t}$ denote the average tangent direction at the vertex computed as $\|\boldsymbol{q}_{2-1}\| \boldsymbol{q}_{1-0} + \|\boldsymbol{q}_{1-0}\| \boldsymbol{q}_{2-1}$. We require that β be small enough such that the tangent vectors $\boldsymbol{q}_{1-0}$ and $\boldsymbol{q}_{2-1}$ are not flipped with respect to $\boldsymbol{t}$. This is achieved by requiring β to be smaller than the positive solution to the equation $\boldsymbol{p}_{1-0} \cdot \boldsymbol{t} + \beta \boldsymbol{d}_{1-0} \cdot \boldsymbol{t} = 0$ and also than the positive solution to the equation $\boldsymbol{p}_{2-1} \cdot \boldsymbol{t} + \beta \boldsymbol{d}_{2-1} \cdot \boldsymbol{t} = 0$.

After evaluating β for all crack front faces and edges, let α be the smaller value between 1 and the smallest β (or a fraction of the smallest β to tolerate roundoff errors) along the crack front. Hereafter, α is denoted as the crack advance limit. If $\alpha = 1$, then there is no local self-intersection in the crack surface after propagation. If $\alpha < 1$, we multiply the crack front advance vectors $\boldsymbol{d}$ by α for all the vertices to obtain a self-intersection-free crack front. We apply this procedure in Step 6 of the algorithm described in Section

4.3.

2.2.3 Crack front update and optimization of crack surface mesh

In crack growth simulations with explicit crack surfaces, the crack surface mesh must be updated as the front is propagated. In this work, we use two techniques, referred to as propagate and extrude (PAE) and propagate and smooth (PAS), respectively. These techniques are illustrated in Figure 3. The details of these techniques as well as the criteria to select them are presented as follows.

Propagate and extrude (PAE) In the first technique, we "extrude" the vertices and edges of the crack front to create a new layer of faces. We create faces in two modes. In the first mode, we first clone a vertex for each vertex on the crack front (cf. Figure 3). The coordinates of these cloned vertices are set to the new crack front position computed in Step 6 of the algorithm presented in Section 4.3. We add an edge between the original and cloned vertices and also between adjacent cloned vertices. These vertices and edges constitute a layer of quadrilaterals. We then divide each quadrilateral into two triangles by adding an edge along a diagonal (such as from upper-left corner to the lower-right corner). This mode preserves the number of vertices on the crack front.

In the second mode, we allow refining the crack front if an edge is longer than some user-specified threshold. In particular, we first create a layer of quadrilaterals as above. If an edge on the new crack front is too long, then we subdivide its corresponding quadrilateral into three triangles by adding a vertex at its mid-point and connecting it with every vertex of the quadrilateral (cf. Figure 3).

After extrusion, the triangles next to the crack front may be poorly shaped if the time step is too small compared to the edge length. These poorly-shaped triangles can adversely affect the accuracy of the computed normal directions of the crack front. To resolve this issue, after generating a layer of faces we further optimize the quality of the mesh. We use the variational smoothing technique presented in [30], which optimizes the triangles against some "ideal" reference triangles by moving the vertices while preserving special features of the surface geometry (such as sharp turns in the crack surface). We refer readers to [30] for more detail about the technique, but hereafter we describe the selection of ideal triangles.

In a typical setting, an ideal triangle is equilateral. However, in PAE the extruded edges are nearly orthogonal to the front, so right triangles are more desirable. For simplicity, if no edge splitting is performed, we set the ideal triangle to be right triangle with a leg ratio of two, so that each extruded edge is about half as long as its incident front edges. If edge splitting is performed, we choose the ideal right triangles to be isosceles. For the triangles in the interior of the crack surface that have no layered structures, we use equilateral triangles as the ideal triangles. To distinguish these different types of triangles, we tag the triangles during extrusion based on their desired shapes and preserve these tags during the course of the simulation.

Propagate and smooth (PAS) PAE adds a layer of faces, so the crack surface would have an excessive number of triangles if it were invoked at every time step. To avoid the problem, we also allow propagating the front by only moving the vertices on the crack front. As in PAE, the coordinates of crack front vertices are updated with the new crack front position computed in Step 6 of the algorithm presented in Section 4.3. After moving vertices on the crack front, we then apply the variational smoothing described above to improve mesh quality. If PAE has been invoked previously, we also use right triangles as the ideal triangles during this variational smoothing to preserve the orthogonality of the extruded edges.

Selection criteria In a typical simulation, we apply both PAS and PAE. PAE is applied when 1) the crack advance is non-planar with respect to the immediate previous step, 2) the crack front advance is not reduced by the crack advance limit procedure, or 3) a crack surface front refinement is needed, i.e. one of the crack front edge lengths reaches a predefined length value limit. Otherwise, we apply PAS.

Interaction with boundary In most of the problems, the crack front is the boundary curve of the crack surface and is closed by definition. However, a crack may be at the boundary of the solid, for which the crack front is only a subset of the boundary curve, namely the subset that "cuts" the solid. Our technique provides some preliminary supports for the interaction of the crack front with solid boundaries. In particular, we allow the user to flag the vertices where the crack front intersects with the solid boundary. In PAE, these vertices are extruded along the material boundary. The border vertices of the crack surface that are not on the crack front are not propagated or extruded, but they are smoothed tangentially along the boundary curve.

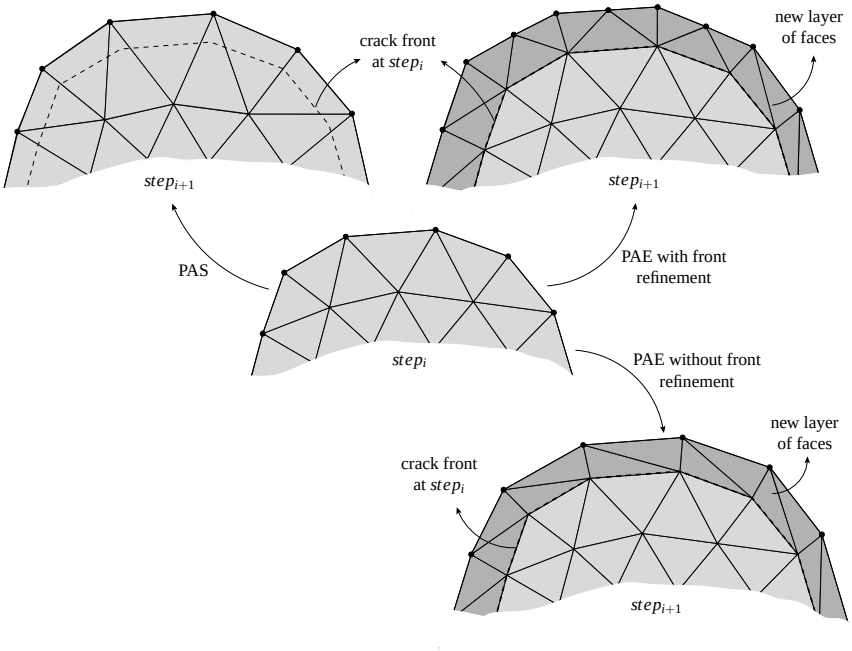

Figure 3: *Crack front update.*

3 Problem description

The methodology presented in Section 2 can be applied to several types of crack growth problems, e.g., dynamic crack propagation, fatigue failure assessment, crack growth with cohesive fracture models, and so on. For simplicity and without loss of generality, the class of problems selected to verify the methodology presented here is the fatigue crack growth in three-dimensional solids. The problem consists of a three-dimensional body subjected to cyclic loading with an existing embedded or surface breaking crack. Figure 4 schematically illustrates our target problem.

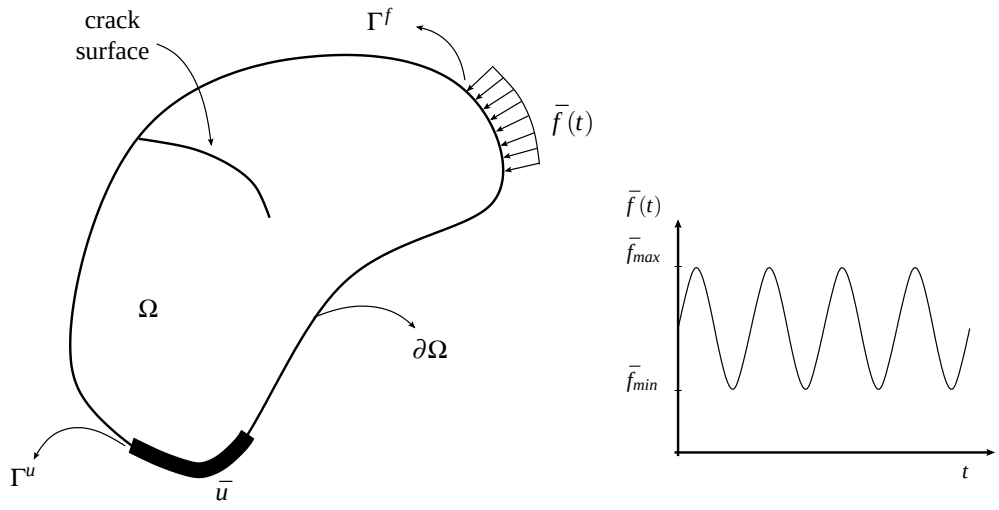

Figure 4: *Fatigue problem.*

Fatigue crack growth analysis is a problem of probabilistic nature which is of great importance in engineering. Most of the equations utilized to describe fatigue crack growth behavior are based on observations of the physical phenomenon and extensive material testing. These equations are crucial for the design of engineering structures in which the assessment of fatigue failure is a major requirement. Some example of these structures include aircrafts, rockets, engines, pressure vessels, and bridges.

Depending on the type of load, material behavior and environmental influences, there are several classes of fatigue behavior [60]. This work focuses on the simulation of stable crack growth under high-cycle fatigue. In the high-cycle fatigue mechanism, the loads are generally low compared with the limit stress of the material, i.e. small-scale yielding occurs. As a consequence, the stress state around the crack front can be fully characterized by linear elastic fracture mechanics. Other assumptions in the high-cycle fatigue problems analyzed in this work include: cyclic loading with constant amplitude, $\bar{f}_{max} > 0$ and $\bar{f}_{min} \geq 0$ (cf. Figure 4) and quasi-static crack growth.

From a macro-scale point of view, high-cycle fatigue can be regarded as a quasi-static phenomenon. Moreover, the crack growth mechanism in high-cycle fatigue can be characterized by linear elastic fracture parameters, e.g. the stress intensity factors [59]. Therefore, a robust and accurate method to analyze linear elastic fracture mechanics problems, such as the *hp*-GFEM presented in Section 2 and described in more details in [50], is essential for a successful fatigue crack growth simulation.

4 Crack growth model

A high-cycle fatigue crack growth simulation is an incremental process in which a sequence of linear elastic fracture mechanics steps is repeated in order to describe the evolution of the crack front. Each increment step is dependent on the crack problem solution and crack front prediction of previously computed steps. Therefore, an accurate solver together with a robust criterion for the crack front advance prediction are required for a successful crack growth simulation.

During the simulation, the crack growth criterion has to be able to provide the amount and direction of crack advance, and the lifetime of the structure. In three-dimensional elastic fracture analysis, the stress

state at the crack tip is fully characterized by the stress intensity factors for modes I, II, and III, i.e. K_I, K_{II}, and K_{III}. They can be used to describe the fatigue crack growth behavior and assess fatigue failure. This section presents the fatigue crack growth model utilized in the present work to drive the evolution of the crack front along the simulation.

4.1 Crack growth direction - Schöllmann's criterion

In three-dimensional mixed-mode crack problems, the crack deflection is represented by a kinking angle and a twisting angle as illustrated in Figure 5. There are only a few criteria to estimate the direction of the crack growth in 3-D. The criteria developed by Sih [64], Pook [52], Schöllmann [62] and Richard [58] are listed as the most important ones. According to a detailed study about three dimensional crack growth criteria presented by Richard et al. in [58], the criteria proposed by Sih and Pook are not able to incorporate the effect of mode III in the first deflection angle, θ_0 (see Figure 5), and, therefore, are not suitable for the prediction of three-dimensional mixed-mode crack growth orientation.

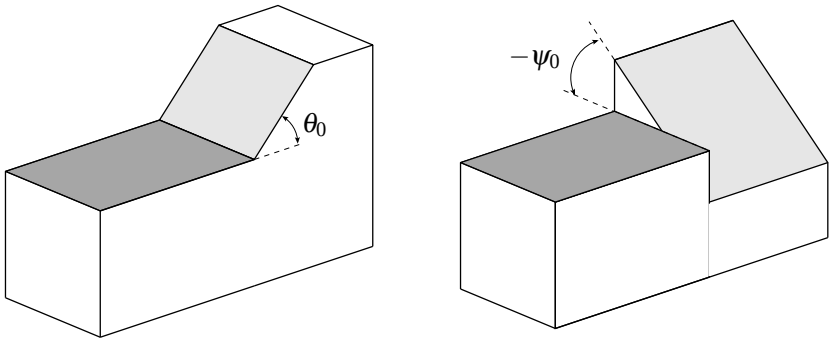

Figure 5: *Crack deflection angles θ_0 and ψ_0 for three-dimensional mixed-mode crack problems [58].*

In this work, Schöllmann's criterion [62] is adopted. A detailed formulation of Schöllmann's criterion can be found in [62]. This criterion assumes that crack growth occurs in the direction of a maximum principal stress $\sigma_1^{'}$, also called *special* principal stress [58]. $\sigma_1^{'}$ is a principal stress where the radial components of the stress tensor are neglected. Such principal stress is determined on a virtual cylindrical surface around the crack front and along a region of interest where the crack growth direction is computed. The maximum principal stress, $\sigma_1^{'}$, is given by the following equation

$$\sigma_1^{'} = \frac{\sigma_\theta + \sigma_z}{2} + \frac{1}{2}\sqrt{(\sigma_\theta - \sigma_z)^2 + 4\tau_{\theta z}^2} \tag{14}$$

where σ_θ and $\tau_{\theta z}$ are the components of the stress tensor obtained by the superposition of all three fracture modes described by the near-front solution in cylindrical coordinates r, θ, and z (cf. Figure 1(b)), given by

$$\begin{aligned} \sigma_\theta &= \frac{K_I}{4\sqrt{2\pi r}}\left[3\cos\left(\frac{\theta}{2}\right) + \cos\left(\frac{3\theta}{2}\right)\right] - \frac{K_{II}}{4\sqrt{2\pi r}}\left[3\sin\left(\frac{\theta}{2}\right) + 3\sin\left(\frac{3\theta}{2}\right)\right] \\ \tau_{\theta z} &= \frac{K_{III}}{\sqrt{2\pi r}}\cos\left(\frac{\theta}{2}\right) \end{aligned} \tag{15}$$

where K_I, K_{II}, and K_{III} are the stress intensity factors for modes I, II and III, respectively. Schöllmann's criterion also assumes that there is no contribution to the kinking angle from σ_z, i.e. $\sigma_z = 0$. The coordinates

r and θ are polar coordinates on the crack front as illustrated in Figure 1(b). According to the assumption of the crack growth direction, the crack deflection angle, θ_0 is determined by

$$\left.\frac{\partial \sigma_1^{'}}{\partial \theta}\right|_{\theta=\theta_0} = 0 \text{ and } \left.\frac{\partial^2 \sigma_1^{'}}{\partial \theta^2}\right|_{\theta=\theta_0} < 0. \tag{16}$$

There is no closed-form solution for the above formulation. Nonetheless, the prediction of the deflection angle, θ_0, can be determined by either an optimization algorithm applied to Equation (14) or a root finder algorithm applied to Equation (16).

Once the first deflection angle θ_0 is determined, the second deflection angle ψ_0 is defined by the orientation of the principal stress $\sigma_1^{'}$ and can be obtained by

$$\psi_0 = \frac{1}{2}\arctan\left[\frac{2\tau_{\theta z}(\theta_0)}{\sigma_\theta(\theta_0) - \sigma_z(\theta_0)}\right]. \tag{17}$$

One can observe that Equation (14) includes the stress intensity factor for mode III, which indicates that Schöllmann's criterion is suitable for simulating three-dimensional cracks under general mixed-mode loading. When $K_{III} = 0$, this criterion is equivalent to the criterion of maximum tangential stress proposed by Erdogan and Sih [20]. Furthermore, Schöllmann's criterion is well-suited for computational implementation of crack growth prediction and has been successfully implemented in standard FEM research codes such as [61].

4.2 Crack front advance and fatigue life prediction - Paris-Erdogan equation

Fatigue crack growth rate is a complex non-linear equation of several variables. Laboratory experiments and observation of structures under service loads have shown that the rate of crack increment with respect to the number of load cycles, da/dN, is a function of the crack length, the state of stress, material parameters, thermal, and environmental effects [65]. There are several empirical fatigue crack growth equations in which all the effects mentioned above can be considered. This work focuses on the fatigue of macro-cracks with cyclic loads of constant amplitude only. The growth equations utilized to describe this type of problem are rather phenomenological than analytical. In the present study, Paris-Erdogan equation [47]

$$\frac{da}{dN} = C\,(\Delta K)^m \tag{18}$$

is used to predict the crack growth rate. In Equation (18), C and m are regarded as material constants, $\Delta K = (1-R)K_{max}$ is the stress intensity factor range in fatigue loading, where R is the ratio of minimum to maximum loads applied in a cycle and K_{max} is the stress intensity factor for the maximum load. In Equation (18), ΔK takes into account mode I only.

In complex three-dimensional loading situations, Equation (18) should consider the mixed-mode effects. For this purpose, ΔK can be replaced by the cyclic comparative stress intensity factor, ΔK_v, given by [58]

$$\Delta K_v = \frac{\Delta K_I}{2} + \frac{1}{2}\sqrt{\Delta K_I^2 + 4(\alpha_1 \Delta K_{II})^2 + 4(\alpha_2 \Delta K_{III})^2} \tag{19}$$

where $\alpha_1 = K_{Ic}/K_{IIc}$ and $\alpha_2 = K_{Ic}/K_{IIIc}$ are the ratios of the fracture toughness of mode I to mode II and of mode I to mode III, respectively. With $\alpha_1 = 1.155$ and $\alpha_2 = 1.0$, the fracture surface provided by Equation

(19) shows good agreement with the fracture surface provided by Schoolman's criterion [58, 62]. Assuming $\Delta K = \Delta K_v$, Equation (18) provides a well-suited correlation between the crack-growth rate and the range of the cyclic comparative SIF for the three-dimensional mixed-mode crack problem presented in Section 3.

In the incremental algorithm for fatigue crack growth, the maximum allowed crack front increment, Δa_{max}, is set at the beginning of each crack step. Since in three-dimensional mixed-mode crack simulation the stress intensity factors may vary along the crack front and the fatigue growth is governed by (18), the increments along the crack front must be applied accordingly. The maximum crack increment size, Δa_{max}, is applied to the crack front vertex that has maximum cyclic comparative stress intensity factor, $\Delta K_{v_{max}}$. The crack growth increments for the remainder of the crack front are computed by using the crack growth rate and the number of cycles of the current step. Thus, for a given crack front vertex j, we have

$$\Delta a_j = C\left(\Delta K_{v_j}\right)^m \frac{\Delta a_{max}}{C\left(\Delta K_{v_{max}}\right)^m} = \Delta a_{max}\left(\frac{\Delta K_{v_j}}{\Delta K_{v_{max}}}\right)^m \tag{20}$$

where ΔK_{v_j} is the cyclic comparative stress intensity factor for the vertex j.

Assuming that the crack growth increment is small with respect to the crack length and other dimensions of the analysis domain, the fatigue life estimate can also be computed in an incremental fashion. The incremental form of Equation (18) for fatigue life prediction is given by

$$N_i = N_{i-1} + \frac{\Delta a_{max}}{C\left(\Delta K_{v_{max}}\right)^m} \tag{21}$$

where N_i and N_{i-1} are the number of cycles in the current and previous steps, respectively.

4.3 Crack growth algorithm

This section describes the crack growth algorithm used in the numerical examples presented in Section 5. The algorithm consists of an incremental process in which, at each step, a small crack advance is prescribed and a linear elastic fracture mechanics problem is solved in order to describe the evolution of the crack front. In the simulation, we assume that an initial crack already exists in the domain of analysis and the parameters C, m, and R for the fatigue life equation (18) as well as the maximum applied load are given. Δa_{max} is set at the beginning of the simulation and can be defined as a function of the increment step i.

The crack growth algorithm is as follows. For each crack increment Δa_i, $i = 0 \ldots n$, do:

1. Solve a linear elastic fracture problem using the *hp*-GFEM and the current representation of the crack surface. The solution is obtained for the maximum load applied to the analysis domain. This step is similar to solving a static problem like the examples discussed in [50]. In this step, *h*-refinement is applied around the crack front for the current position of the crack front. In the next crack increment, the mesh is unrefined until its initial configuration and a new *h*-refinement is applied around the new position of the crack front. Hence, the mesh is always adapted to the current crack front position. In a similar fashion, the non-uniform *p*-enrichment presented in [50] can also be applied as the crack front evolves.

2. Compute the stress intensity factors (SIF) for modes *I*, *II* and *III* for each vertex along the crack front for the maximum cyclic load, i.e. $K_{I_{max}}$, $K_{II_{max}}$, $K_{III_{max}}$. The SIF can be extracted from the *hp*-GFEM solution using, e.g., the contour integral method (CIM) or the cut-off function method (CFM) [49, 72, 73].

3. Compute the deflection angles θ_0 and ψ_0 for each vertex along the crack front based on the SIF values computed at Step (2). The equations used in this step are presented in Section 4.1. One can note that this step could be computed using either the maximum SIFs or the minimum SIFs because the equations used in the computation of the deflection angles using the maximum SIFs or the minimum SIFs differ only by a constant.

4. Compute the cyclic comparative SIF variation using Equation (19).

5. Compute the crack increment for each vertex along the crack front using Equation (20).

6. While proposed crack front position is not geometrically feasible, i.e. $0 < \alpha < 1$:

   (a) Compute advance vectors, $\boldsymbol{d}_j$ (cf. Figure 2), for all crack front vertices. These advance vectors are computed using the results obtained from Steps (3) and (5). If available, the advance limit parameter, α, computed in Step (6b) is applied to scale down the advance vectors. The deflections and the crack increment for each vertex as well as the advance limit parameter provide the new crack front position.

   (b) Use FOM to estimate the crack increment limit to prevent self-intersections

   - If the crack increment exceeds the limit, return the estimated advance limit parameter, α, and go to Step (6a) to provide new advance vectors for the crack vertices. Section 2.2.2 describes the procedure to compute the advance limit parameter.
   - Otherwise, update crack front position using either PAE or PAS and **break** while loop. Section 2.2.3 describes the details of the crack front updates PAE and PAS.

7. $i = i+1$ and if $i < n$, go to Step (1), otherwise, **stop**.

A similar sequence of steps is also performed in the research codes that use the standard FEM for fatigue crack growth assessment such as FRANC3D [8], ADAPCRACK3D [61] and Zencrack [80]. The main difference is that, in this work, we explore the flexibility of the *hp*-GFEM to efficiently build accurate approximations at each crack step and evolve the crack surface without the mesh topology issues usually found in crack growth simulations with standard FEM [77]. Another important feature of the proposed approach is that the FOM is applied along the crack front to predict eventual self-intersections and to ensure geometrically feasible crack front descriptions for each crack growth step.

5 Numerical examples

This section presents numerical analyses of three-dimensional fatigue crack growth problems using the algorithm presented in Section 4.3. The numerical examples are solved using the *hp*-GFEM with the refinement and enrichment recommendations as well as the crack surface representation presented in [50, 51]. At each crack increment in all examples, a static crack problem is solved with polynomial order $p = 3$ for both continuous and discontinuous components of the solution (Equation (9)), crack front enrichment (Equation (10)), and localized crack front refinement of $L_e/a_o \simeq 10^{-2}$, where L_e is the size of a tetrahedron element on the crack front and a_o is the initial characteristic crack length.

5.1 Crack front self-intersection verification for FOM - Non-convex crack front

This example consists of a planar surface-breaking crack with non-convex crack front in a prism. Figure 6 illustrates the initial coarse tetrahedral mesh and the initial crack surface description. The geometric parameters of the problem are $L/a_o = 2$, $a_o/b_o = 2$, and $a_o/t = 1$. $E = 2.0 \times 10^5 MPa$ and $\nu = 0.30$ are Young's Modulus and Poisson's ratio, respectively. The prism is subjected to a uniform tension cyclic load, $\sigma(t)$, on top and bottom surfaces of the domain as illustrated in Figure 6. The fatigue parameters are $C = 1.463 \times 10^{-11} MPa^{-2.1} m^{-0.05}/cycle$, $m = 2.1$, $\sigma_{max} = 1MPa$ and $R = 0$.

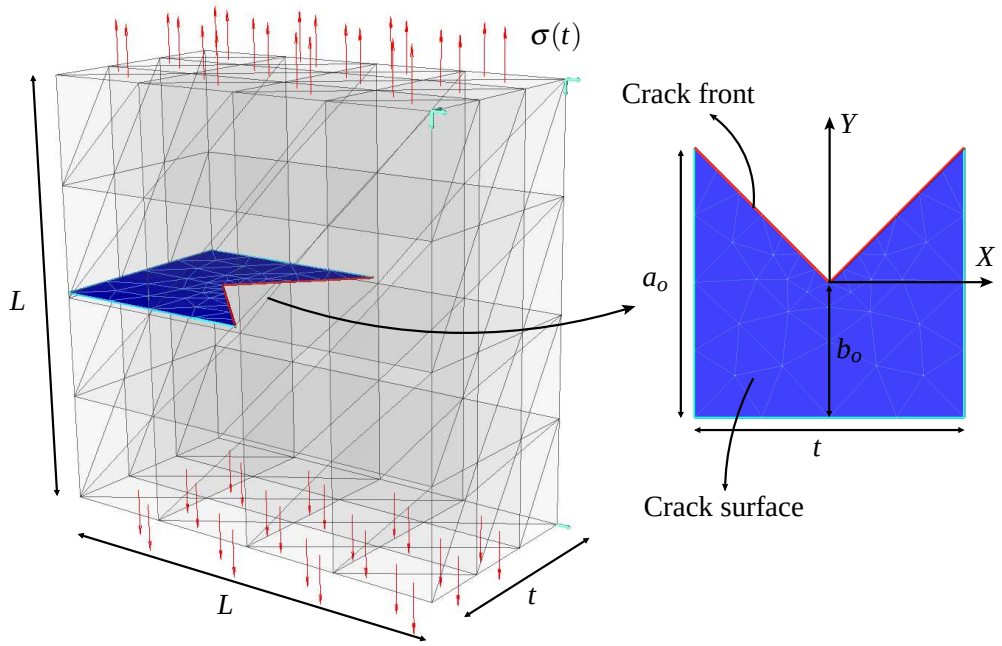

Figure 6: *Non-convex crack front example - model description.*

In this example, self-intersection of the crack front is imminent. The main goal here is to verify the face offsetting method (FOM) for crack growth. The FOM provides geometrically feasible crack front descriptions by setting the crack advance limit that prevents self-intersection of the crack front. This simulation is performed with $n = 19$ incremental steps and the maximum increment size is $\Delta a_{max} = 0.05 a_o$.

This example is subjected only to mode I throughout the simulation. In general, the effects of fatigue tend to smooth out the crack front curvature such that the variation of the stress intensity factor K_I is reduced. Moreover, this simulation is likely to present the crack front tunneling effect, i.e. a curved crack front configuration due to the variation of stress intensity distribution caused by the domain boundary.

Figure 7(a) shows the crack front position for each step of the fatigue crack growth simulation. The crack front geometry is smoothed out due to the fatigue process. In this case, the crack front middle propagates faster than the crack front ends. In addition, the tunneling effect is also observed after the crack front becomes straight. Figure 7(b) plots the normalized mode I stress intensity factors along the crack front for all steps during the simulation. The normalized stress intensity factor is defined as

$$\bar{K_I} = \frac{K_I}{\sigma\sqrt{\pi a_o}}. \tag{22}$$

As expected, the results show that the stress intensity factors are smoothed out due to the fatigue process.

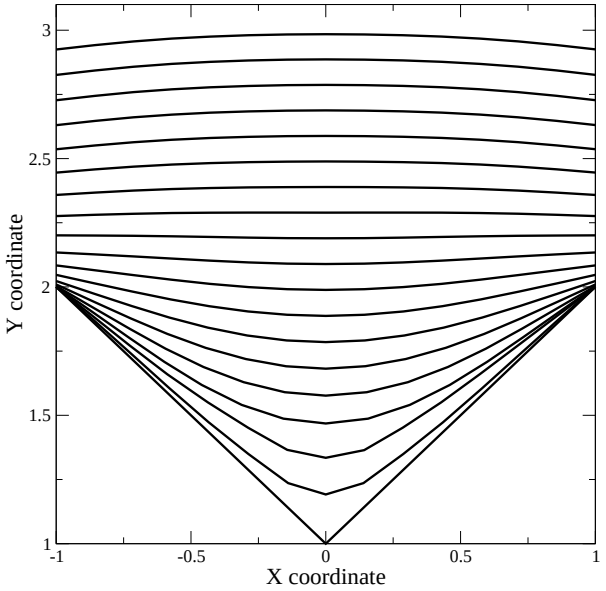

(a) Growth of planar crack with non-convex crack front in a prism.

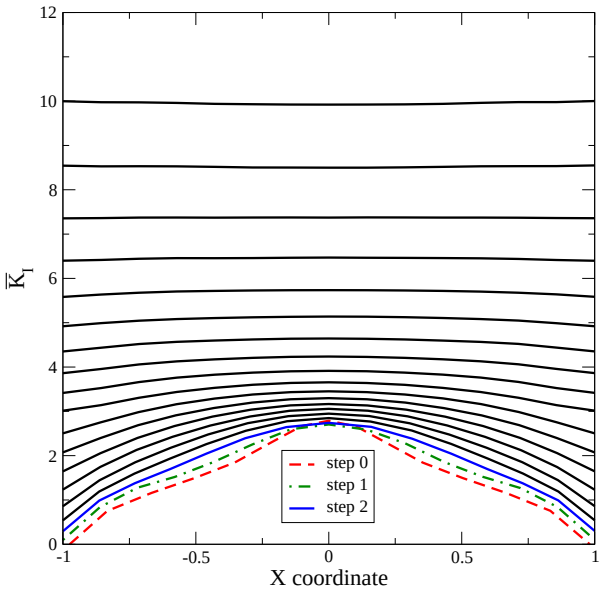

(b) Normalized mode *I* stress intensity factors for all crack growth steps.

Figure 7: *Crack front configurations and SIF values along the crack front for non-convex crack front.*

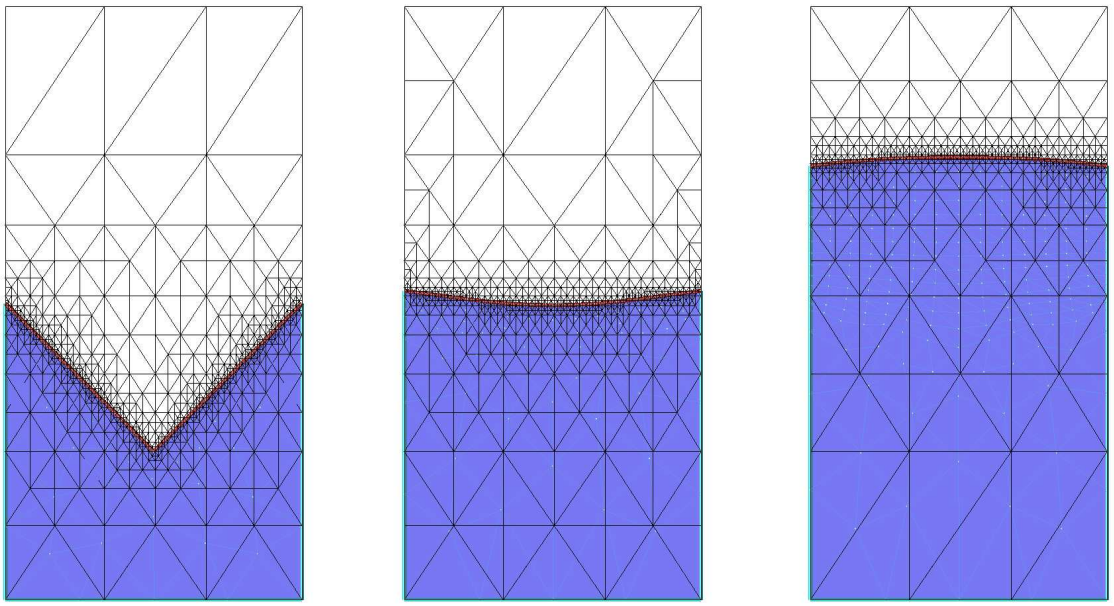

(a) Step 0. (b) Step 8. (c) Step 18.

Figure 8: *Non-convex crack front - localized mesh refinement around the crack front for three crack steps (top view).*

The main goal of this example is to trigger the FOM self-intersection detection during the simulation.

In the first step of the simulation, FOM predicted the self intersection and the crack increment was reduced to $\Delta a_{limit} = 0.93\Delta a_{max}$. This detection scheme prevents the creation of voids in the crack front and provides geometrically feasible crack front representations throughout the simulation. The crack front geometry results presented in Figure 7(a) are as expected. These results ensure that the FOM techniques applied to track the crack front evolution do not affect the physics of the problem.

Adaptive high-order discretizations are automatically built for each crack step during the crack growth simulation. These high-order discretizations are easily built using the *hp*-GFEM since the volume mesh need not fit the crack surface. Localized mesh refinement and unrefinement are applied along the crack front in order to provide a mesh refinement that follows the position of the crack front throughout the simulation. Figures 8 and 9 illustrate the localized refinement applied along the crack front and a planar cut through the mesh showing the von Mises stress at the mid front for steps 0, 8 and 18, respectively.

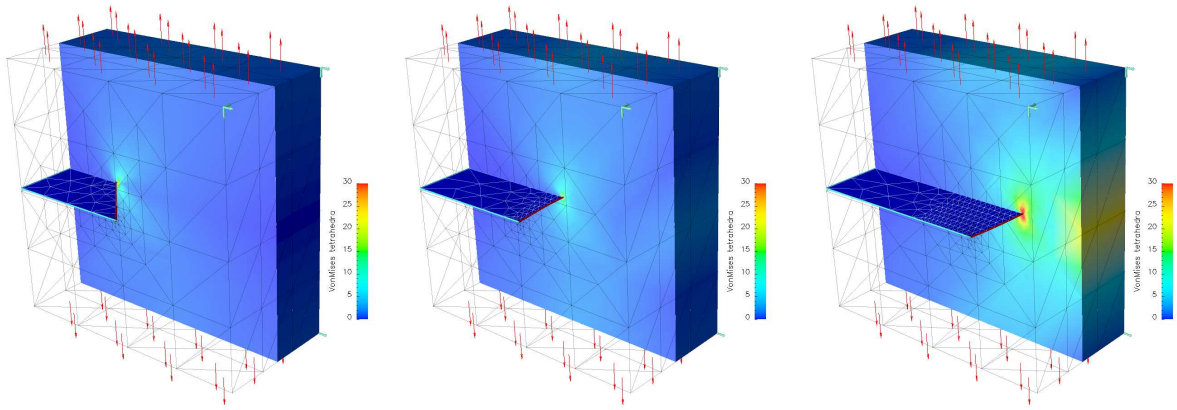

(a) Step 0. (b) Step 8. (c) Step 18.

Figure 9: *Non-convex crack front - cut through von Mises stress solution at mid front (off diagonal view).*

5.2 Validation against experimental results

This example consists of the fatigue simulation of a plate containing an inclined crack as illustrated in Figure 10. The geometry of the plate model and the experimental data for the position of the crack front throughout the simulation are provided in [55]. The material used for the plate specimen is the titanium alloy $Ti-6Al-4V$. The cyclic load applied in the experiment is $\sigma_{max} = 172.37MPa$ with ratio of the minimum to the maximum tensile loads $R = 0.1$. According to [55], the maximum tensile load is selected such that the radius of the plastic zone around the crack front is approximately $0.25mm$, i.e less than 10% of the specimen thickness, therefore, the assumption of small scale yielding applies.

Figure 10 shows the dimensions of the model. In [55], the dimensions used in the specimens are $h = 102.4mm$, $w = 38.1mm$, $t = 3.175mm$ and $a = 6.73mm$. The slope of the crack with respect to the y-axis is $\beta = 43^\circ$ (see Figure 10). To apply the cyclic load, the machine utilized in the experiments required two sets of holes on the top and bottom regions of the plate height. Due to the lack of information about the dimensions of the plate holes used in the experiments and in order to be able to assume a uniformly distributed load at the ends of the plate, we adapted a plate model with a smaller height. As such, the height of the plate model is set to be $2/3$ of the height of the specimen and all other dimensions are the same. Since the variation of the crack front increment through the thickness of the plate is not a concern

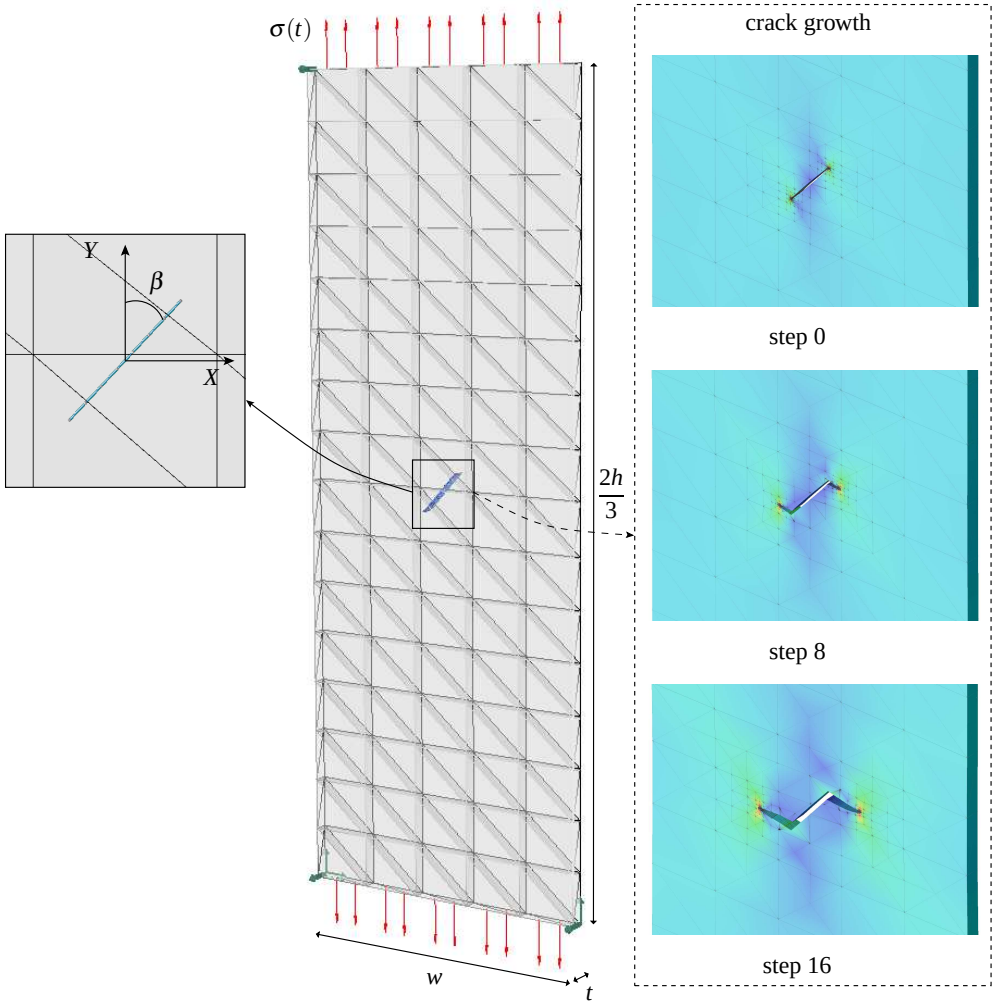

Figure 10: *Inclined crack model and crack growth steps.*

in this simulation, we assume that the crack front remains straight throughout the simulation and the SIF values along the front are constant and equal to the SIF values in the middle of the front. In [55], the material parameters and the parameters for Paris-Erdogan equation (18) are not provided. In the numerical simulation, we use Young's modulus, $E = 115 \times 10^3 N/mm^2$, and Poisson's ratio $\nu = 0.32$ as material parameters and $C = 1.251 \times 10^{-11} (N/mm^2)^{-2.59} mm^{-0.295}/cycle$ and $m = 2.59$ as Paris-Erdogan equation parameters for the titanium alloy $Ti-6Al-4V$. These parameters can be found in [1].

Figure 11 illustrates the GFEM mesh discretization for three steps of the inclined crack growth simulation. The proposed approach facilitates the automatic construction of strongly graded meshes around the crack fronts along the simulation. Localized h-refinement is applied to the elements that intersect the crack front. After propagating the crack fronts, the mesh is unrefined to its initial coarse configuration (cf. Figure 10) and a new refinement is applied to the elements that intersect the new crack fronts in their new positions. This procedure reduces the computational cost of the simulation by avoiding unnecessary degrees of freedom in the discretization. The same procedure cannot be applied when the volume mesh is used to represent the crack surface as in level set methods. In these approaches, all elements that intersect

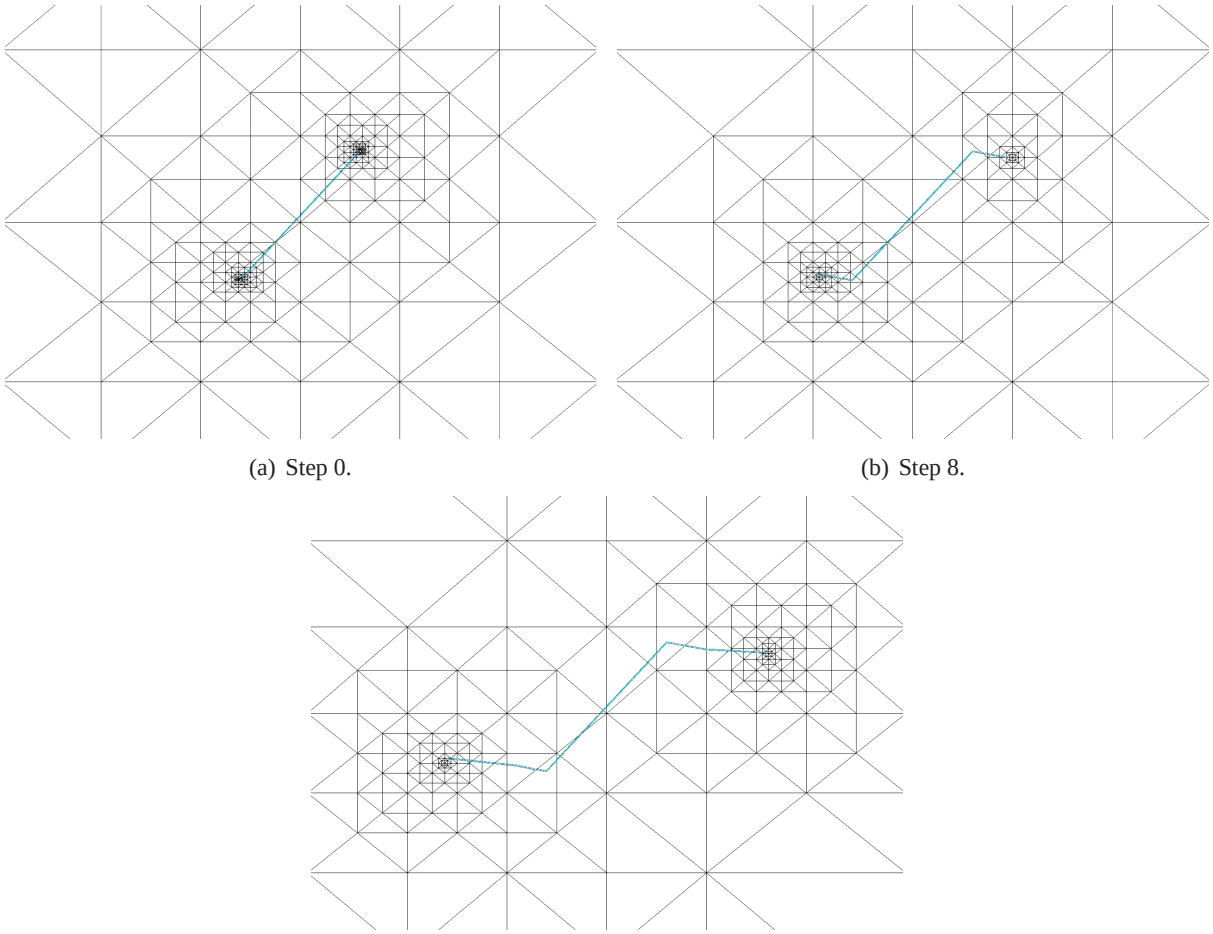

(a) Step 0. (b) Step 8.

(c) Step 16.

Figure 11: *Inclined crack - localized mesh refinement around the crack fronts for three crack steps (front view).*

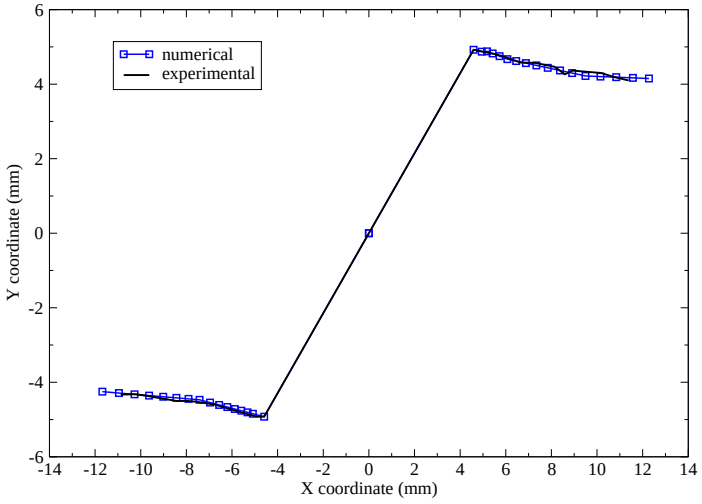

Figure 12: *Front view of crack configuration - experimental* vs. *numerical.*

the crack surface may have to be refined in order to provide an accurate crack surface representation. As an example, the representation of the crack turn shown in Figure 11(c), requires a fine mesh around the crack turning point.

In the proposed methodology, no volume mesh refinement is required to represent the special features of the crack surface in the simulation. As illustrated in Figure 10, the proposed crack surface representation is able to model the sharp turn in crack direction at the beginning of the simulation and keep this feature of the crack surface throughout the simulation.

Figure 12 plots the crack front X and Y global coordinates using the experimental data provided by [55] and the numerical results. The coordinates from the numerical results are based on the position of the middle of the crack front during the simulation. The numerical results for the prediction of the crack path show good agreement with the experimental results.

5.3 Verification of robustness - Wavy crack front

This example considers a planar crack with planar perturbations along the crack front, hereafter, referred to as wavy crack. The analysis domain is a cube with dimension $2L$ and subjected to a uniform tension cyclic load of maximum magnitude $\sigma_{max} = 1MPa$ perpendicular to the plane of the crack surface, i.e. z-direction, as illustrated in Figure 13. The geometric parameters of the crack surface are $a_0/L = 0.25$, $n_{wave} = 6$, $\Delta a_{max} = 0.035a_0$, and $\varepsilon = 0.1$, where a_0 is the radius of the reference penny-shaped crack, n_{wave} is an integer parameter that defines the number of waves along the crack front, and ε is the crack front geometry perturbation with respect to a penny-shaped crack. The fatigue parameters are $C = 1.463 \times 10^{-11} MPa^{-2.1} m^{-0.05}/cycle$, $m = 2.1$, and $R = 0$. This simulation is performed with $n = 30$ incremental steps. $E = 1.0 \times 10^3 MPa$ and $\nu = 0.30$ are Young's Modulus and Poisson's ratio, respectively. The main objective of this numerical example is to show the evolution of the crack front geometry during the fatigue process.

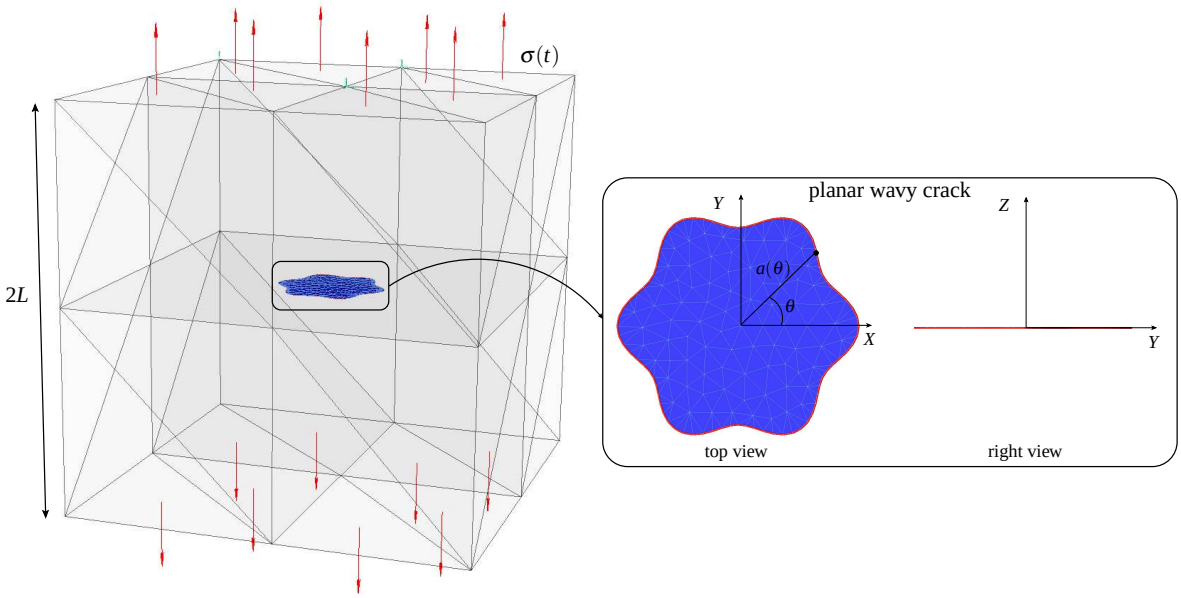

Figure 13: *Wavy crack model description.*

In this case, the crack surface is planar and perpendicular to the direction of the applied load and, therefore, the crack is subjected only to mode I throughout the simulation. According to [10], experimental observations indicate that the effects of fatigue tend to smooth out the crack front curvature such that the variation of the stress intensity factor K_I is minimized. Gao and Rice [22] presented a first-order accurate solution for planar quasi-circular tensile cracks. In the case of wavy cracks whose front is described by

$$a(\theta) = a_0 \left[1 + \varepsilon \cos(n_{wave}\theta)\right] \tag{23}$$

the asymptotic solution for stress intensity factors $K_I^{asym.}$ is given by

$$K_I^{asym.}(\theta) = K_I^{\infty}(a(\theta)) \left[1 - \varepsilon \frac{n_{wave}}{2} \frac{a_0}{a(\theta)} \cos(n_{wave}\theta)\right] \tag{24}$$

where θ is a parametric coordinate along the crack front, as illustrated in Figure 13, and $K_I^{\infty}(a)$ is the stress intensity factor for a penny-shaped in an infinite domain, which is given by

$$K_I^{\infty}(a) = \sigma\sqrt{\frac{a}{\pi}}. \tag{25}$$

One can observe that K_I^{∞} varies along the crack front. Lai et al. [34] presented a static solution of this problem, i.e. n=0, using the boundary element method. A crack growth simulation using the XFEM coupled with fast marching method was presented by Sukumar et al. in [69].

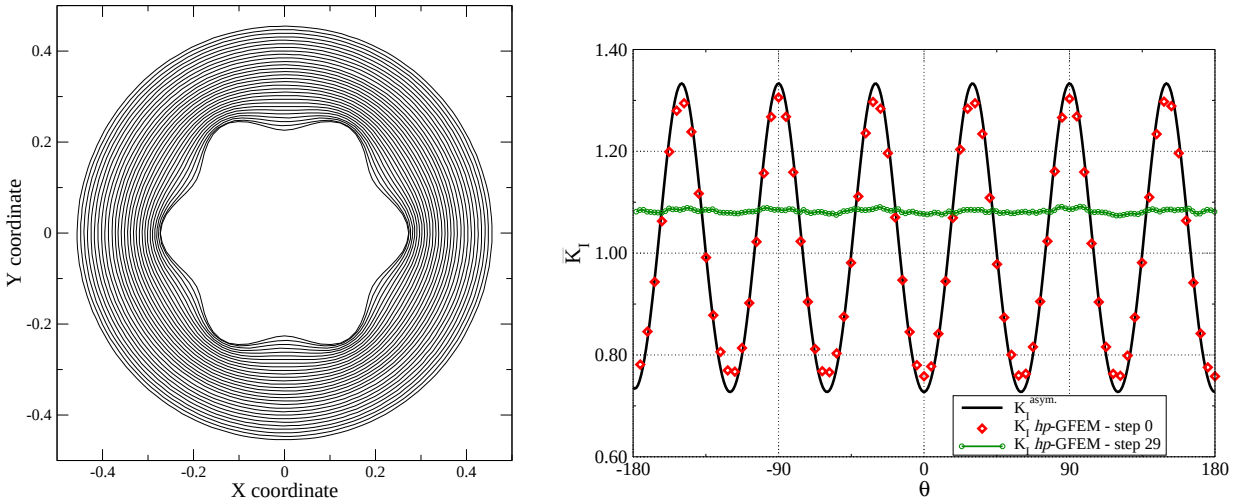

(a) Growth of a wavy crack embedded in a cube.

(b) Mode I stress intensity factors for initial and final crack growth steps.

Figure 14: *Crack front configurations and SIF values along the crack front for wavy crack.*

Figures 14(a) and 14(b) plot the crack front position for all steps during the simulation and the normalized mode I stress intensity factor for the first, $\bar{K}_I^{first}$, and last, $\bar{K}_I^{last}$, steps of the simulation, respectively. The normalized stress intensity factor is defined as

$$\bar{K}_I^{step} = \frac{K_I^{step}}{K_I^{\infty}(a(\theta))} \tag{26}$$

where $step$ is either the first or last step of the simulation. The results show that the wavy crack eventually grows to a penny-shaped crack, which corroborates experimental observations. The ratio of the maximum to the minimum radii of the crack front at the beginning and at the end of the simulation are $a_{max}^{first}/a_{min}^{first} = 1.2$ and $a_{max}^{last}/a_{min}^{last} = 1.004$, respectively. As expected, the variation of the SIFs is smoothed out as the crack evolves. The ratio of the maximum to the minimum SIFs at the beginning and at the end of the simulation are $K_{max}^{first}/K_{min}^{first} = 1.64$ and $K_{max}^{last}/K_{min}^{last} = 1.01$, respectively.

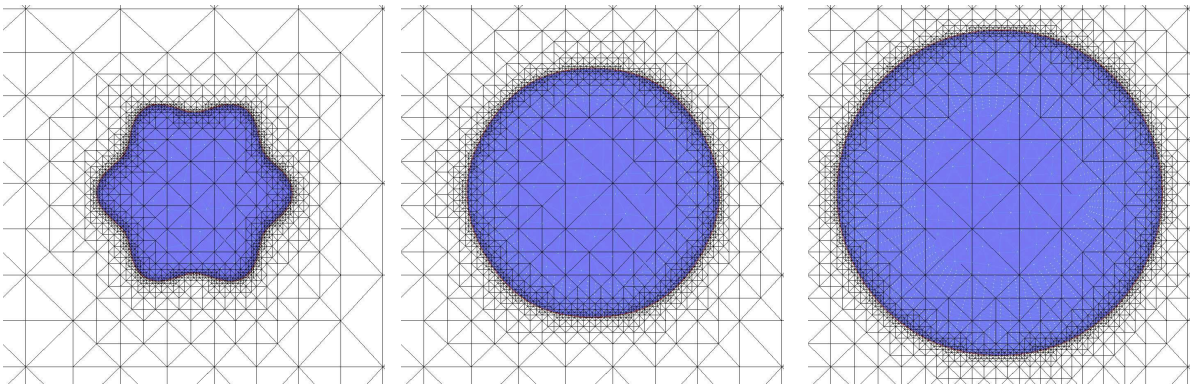

(a) Step 0. (b) Step 15. (c) Step 29.

Figure 15: *Wavy crack - localized mesh refinement around the crack front for three crack steps (top view).*

Figure 15 shows the GFEM mesh discretization for three steps of the wavy crack growth simulation. The *h*-adaptive refinement and unrefinement procedure described in Section 5.2 is also applied in this example. One can observe that the refinement along the crack front follows the crack front position throughout the simulation.

5.4 Crack growth under mixed-mode - Inclined penny-shaped crack

This example consists of an inclined penny-shaped crack in a cube with dimension $2L$. The cube is subjected to a uniform tension cyclic load of maximum magnitude $\sigma_{max} = 1MPa$ along the y-direction, as illustrated in Figure 16. The initial coarse mesh and the initial crack surface configuration are also illustrated in Figure 16. The geometric parameters of the crack surface are $a_0/L = 0.1$ and $\beta = \pi/4$, where a_o is the radius of the initial crack and β is the slope with respect to the yz-plane. The maximum crack front increment allowed in each step is $\Delta a_{max} = 0.02a_0$. In this case, the simulation is performed with $n = 38$ incremental steps. The fatigue parameters are $C = 1.5463 \times 10^{-11} MPa^{-2.1} m^{-0.05}/cycle$, $m = 2.1$, and $R = 0$. $E = 1.0 \times 10^3 MPa$ and $\nu = 0.30$ are Young's Modulus and Poisson's ratio, respectively. The main objective of this numerical example is to show the evolution of the crack surface geometry during the fatigue process.

According to experimental observation in fatigue crack growth, cracks tend to grow in a direction that provides mode I dominance. In the inclined penny-shaped case, the fatigue process imposes a twist to the crack front in order to make it perpendicular to the applied load. In addition, the crack front tends to remain circular throughout the simulation. This example is a mixed-mode problem in which all three modes are

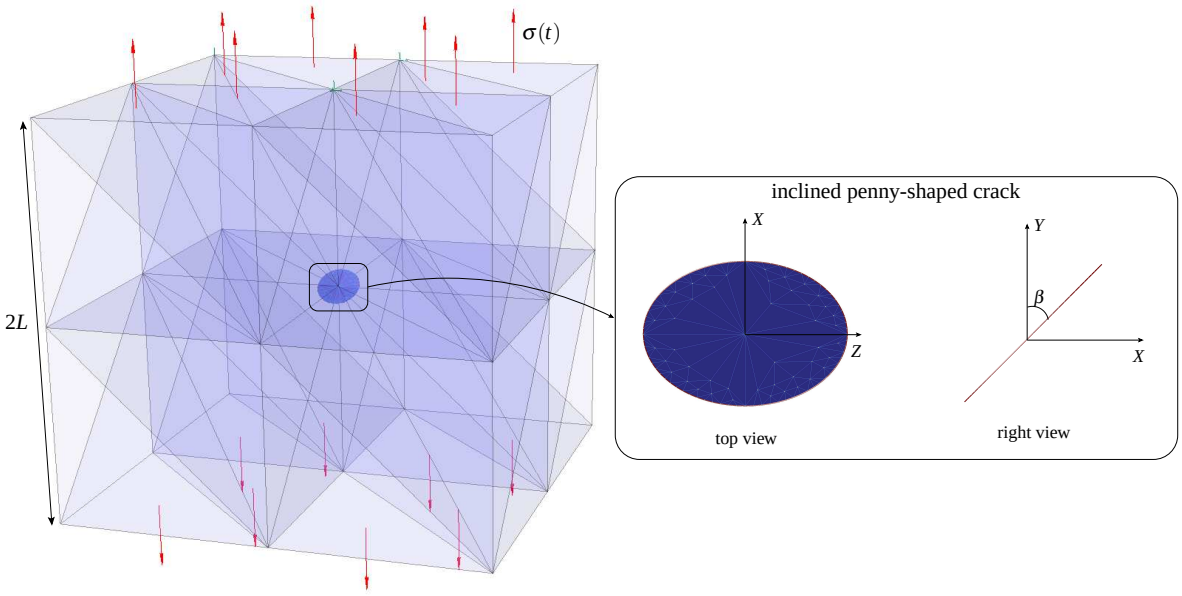

Figure 16: *Inclined penny-shaped crack model description.*

present. The stress-intensity factors along the crack front in an infinite domain are given by [74]

$$\begin{aligned} K_I^{inf.} &= \frac{2}{\pi}\left[\sigma sin^2(\beta)\right] \\ K_{II}^{inf.} &= \frac{4}{\pi(2-\nu)}\left[\sigma sin(\beta)\cos(\beta)\right] cos(\theta)\sqrt{\pi a} \\ K_{III}^{inf.} &= \frac{4(1-\nu)}{\pi(2-\nu)}\left[\sigma sin(\beta)\cos(\beta)\right] sin(\theta)\sqrt{\pi a}. \end{aligned} \tag{27}$$

where θ is an angular coordinate on the crack plane that represents a position on the crack front. The same problem was solved by Gravouil et al. in [26] with the XFEM coupled with the level set method and by Sukumar et al. in [69] with the XFEM coupled with the fast marching method.

Figures 17(a) and 17(b) plot the variation of the SIFs along the crack front for the first and last steps of the simulation, respectively. One can observe that the stress intensity factors (SIFs) for modes *I*, *II*, and *III* in step 0 show good agreement with the SIFs for infinite domain, which ensures an accurate crack front prediction for the next step. We can also observe that the SIF values for modes *II* and *III* vanish and the SIF for mode *I* becomes dominant towards the end of the simulation.

Figures 18 and 19 show the top views of mesh refinement and off left views of the crack surface representation, respectively, at different incremental steps. As the crack evolves, we can observe that the crack front tends to become perpendicular to the axis of the applied load while keeping a circular shape. These results also show that there is no need to *a priori* refine the mesh in the region of potential crack growth, as proposed in [7]. This procedure would lead to substantial increase in problem size of this example due to the nonplanar crack surface path.

Figure 20 shows a cut through the solution at different incremental steps. Thanks to the volume mesh independence of the explicit crack surface representation adopted here and the integration subelements for non-planar cracks presented in [50], the crack surface can assume an arbitrary shape inside of a volume

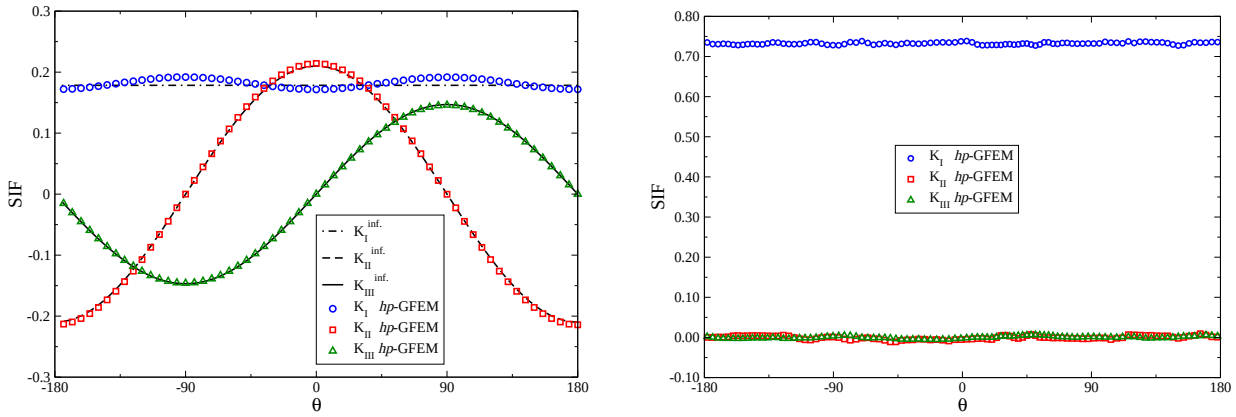

(a) Step 0. (b) Step 37.

Figure 17: *SIFs variation along the crack growth simulation for inclined penny shaped crack.*

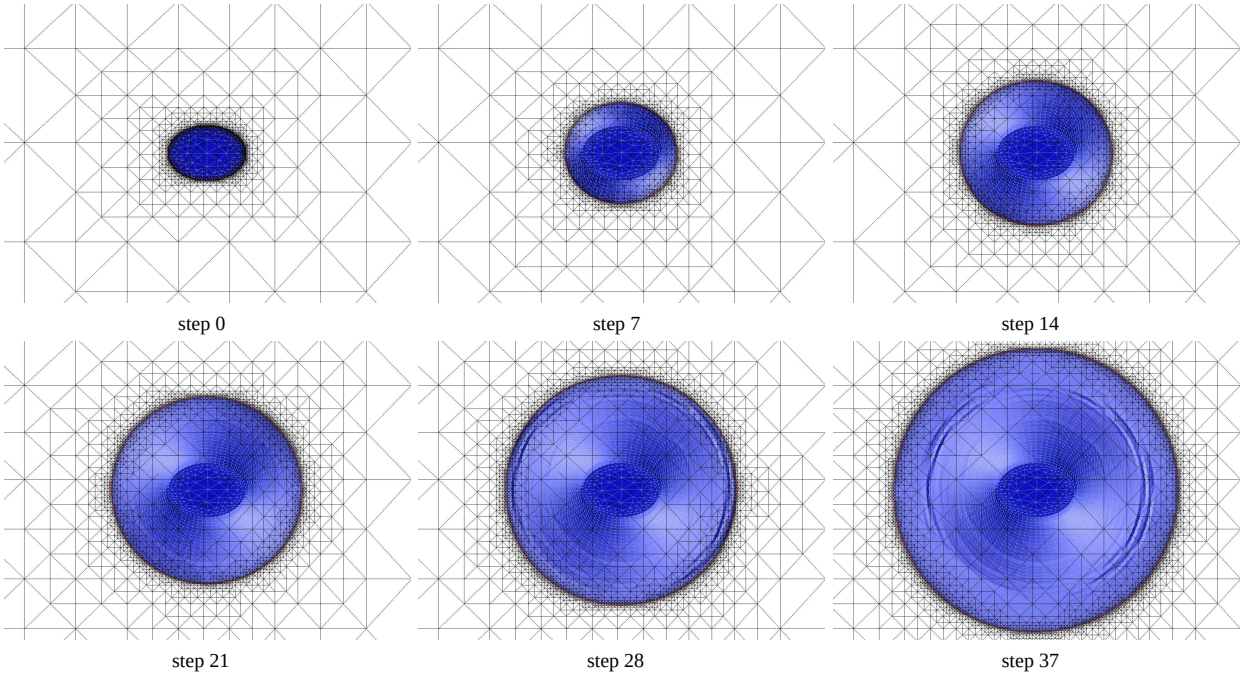

Figure 18: *Inclined penny-shaped crack - localized mesh refinement around the crack front at various crack growth steps (top view).*

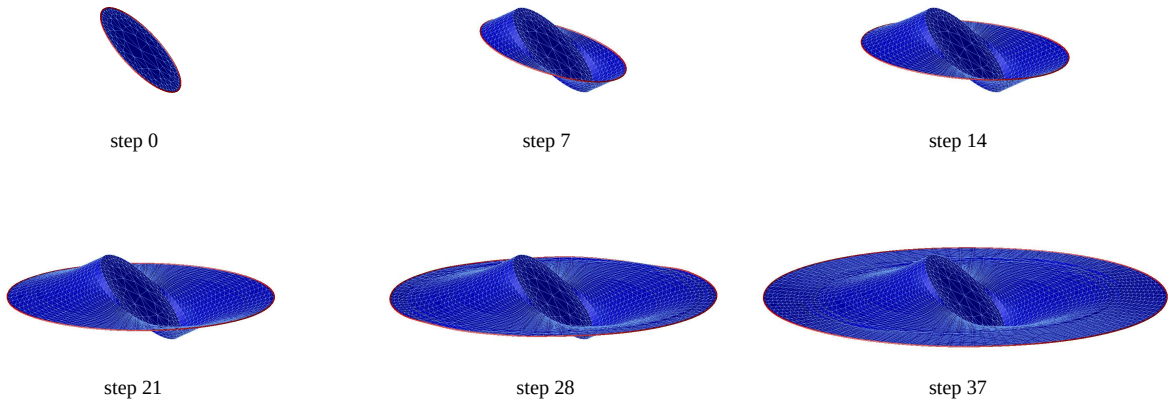

Figure 19: *Inclined penny-shaped crack - crack surface representation at various crack growth steps (off left view).*

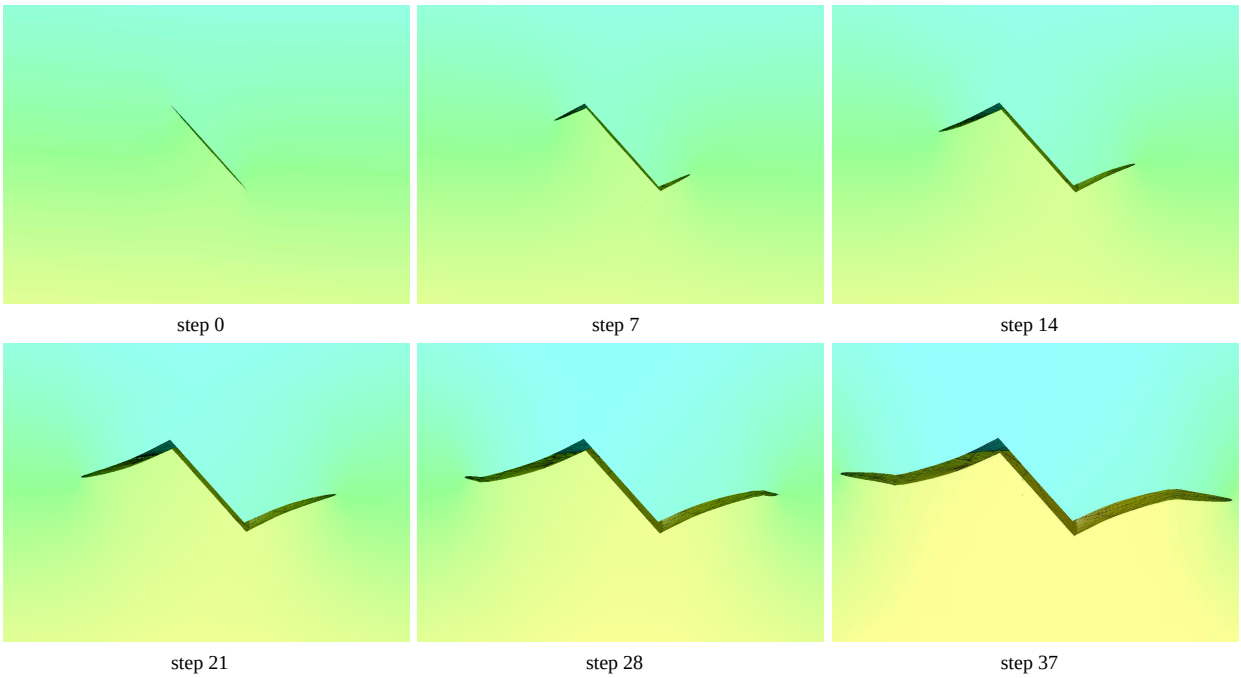

Figure 20: *Inclined penny-shaped crack - cut through solution mesh at the center of the domain at various crack growth steps (off left view).*

mesh with large elements. Moreover, special features of the crack surface, such as sharp turns, can be represented with high fidelity regardless the sizes of the elements of the volume mesh. This feature may not be important for the overall solution of the present problem, however, an accurate description of the crack surface is crucial for crack problems in which the physics is dependent on the crack surface description. Some examples of problems with crack surface dependent physics are crack growth driven by hydraulic pressure applied to the crack surface, crack growth with cohesive models, cracks under compressive loads and so forth.

Again, the *hp*-GFEM discretizations are automatically built at each crack step (cf. Figure 18). Mesh refinement and unrefinement is applied along the crack front in order to provide a localized refinement that automatically follows the crack front throughout the simulation. In contrast with standard FEM techniques, this process does not introduce additional computational cost to the simulation since there are no requirements for the volume mesh to be conforming with the crack surface.

Mode *III* effects on crack path The effects of mixed modality on fatigue crack growth orientation and, consequently, on the crack surface shape have been the main subject of study of several researchers for many years. A detailed literature survey of mixed mode fatigue crack growth can be found in [56]. The crack orientation for mixed mode problems with modes *I* and *II* is very well understood. Erdogan-Sih's [20] criterion, also called maximum tangential stress criterion or hoop stress criterion, is widely used for crack path prediction in two dimensional simulations. However, three-dimensional effects on the orientation of mixed mode fatigue crack growth is not fully understood. The effects of mode *III* in mixed mode fatigue crack growth are discussed and formulated in the works of Pook [52, 53], Schöllmann et al. [62], and Richard et al. [58].

In general, computational simulations for three-dimensional crack growth found in literature do not consider mode *III* effects in the prediction of the crack path. Although Erdogan-Sih's [20] criterion considers only modes *I* and *II* to predict the crack growth orientation, this criterion is broadly applied in three-dimensional simulations to provide the growth direction along the crack front. The works of Carter et al. [8], Krysl et al. [33] and Gravouil et al. [26] are among the works that apply Erdogan-Sih's criterion for crack growth orientation in three-dimensional simulations.

Figure 21 illustrates the results for the same inclined penny-shaped crack example presented in this Section with the crack growth methodology proposed in this paper but considering $K_{III} = 0$ in Equations (16) and (17), which is equivalent to applying Erdogan-Sih's [20] criterion for crack growth orientation. By comparing Figure 19 and Figure 21(a), one can observe that the simulation without mode *III* effects does not provide a planar mode *I* crack growth after 38 crack growth steps. Indeed, Figures 21(b) and 21(c) show that mode *III* stress intensity factors are not completely vanished at the end of the simulation. The mode *III* stress intensity factor values are reduced by only 58% of their initial values at step 0.

Gerstle [25] proposed a criterion that extends Erdogan-Sih's [20] criterion to three dimensional simulations by considering an equivalent mode *I* stress intensity factor which combines modes *I* and *III*. This criterion was applied in three dimensional crack growth simulations with boundary element method (BEM) by dell'Erba and Aliabadi [11] and with FEM by Okada et al. [44]. As observed by dell'Erba and Aliabadi [11], crack growth simulations with this criterion do not show significant reduction in the mode *III* stress intensity factors after several crack growth steps.

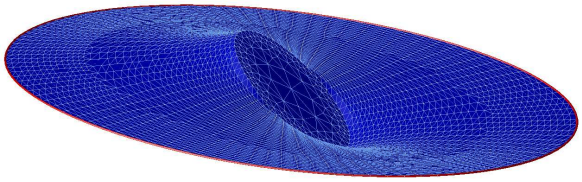

(a) Crack surface at step 37 (off left view).

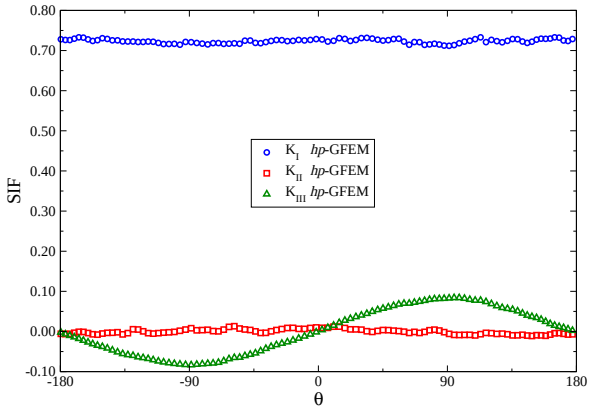

(b) SIFs along crack front at step 37.

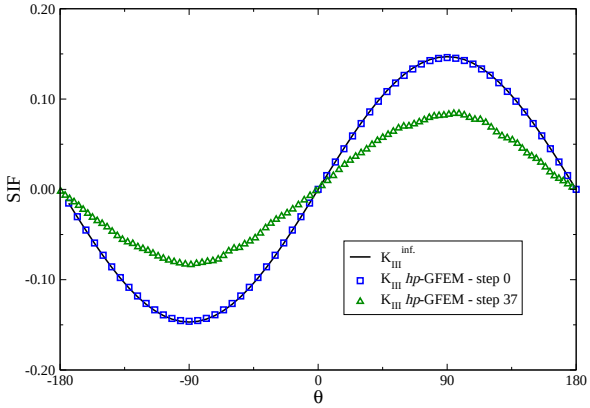

(c) Mode *III* SIFs along crack front at steps 0 and 37.

Figure 21: *Inclined penny shaped crack results for crack growth orientation without K_{III} effects.*

6 Concluding remarks

This paper presents a robust methodology for modeling three-dimensional crack growth simulations of crack surfaces with arbitrary shapes. The proposed methodology is based on the *hp*-GFEM for fracture mechanics [50] to automatically build high-order discretizations coupled with the FOM [29] to track the evolution of the crack front. The verification and validation presented in Section 5 are focused on the analysis of fatigue crack growth, however, the *hp*-GFEM coupled with FOM can be extended to other applications, e.g., dynamic crack growth and crack growth with cohesive elements.

Fatigue crack growth is modeled as a sequence of linear elastic fracture mechanics (LEFM) solutions. Based on the LEFM solutions, Schöllmann's criterion and Paris-Erdogan's equation provide the direction and amount of crack advance, respectively. High-order discretizations with adaptive crack front refinement are automatically generated at each crack step. The *hp*-GFEM presented in [50] is utilized to solve static crack problems at each crack step of the simulation. This process ensures accurate SIFs along the crack front and, consequently, accurate crack growth surface path prediction.

FOM guarantees the geometrical feasibility of the crack surface representation. The FOM is a numerical technique for tracking the evolution of explicit surfaces [29]. In this work, the FOM is applied to track the

evolution of the crack front throughout the crack growth simulation. At each crack growth step, the FOM verifies the crack front advance and, if necessary, provides the advance limit that prevents self-intersections of the crack front.

The proposed methodology provides very accurate crack path description. Prediction of crack growth corroborates experimental data and experimental observations as presented in Section 5. This methodology also allows the crack surface to grow arbitrarily inside of volume meshes with non-uniform refinement. The results presented in Section 5.4 show that crack growth simulations with explicit crack surface representation do not require *a priori* refinement of the volume mesh in the region of potential crack growth. A combination of an explicit crack surface representation and non-planar cuts inside of elements, proposed in [50] for static cracks, results in a powerful tool that allows the representation of arbitrarily continuous cracks with non-smooth surfaces in crack growth simulations. Non-smooth crack surfaces are very common in mixed mode crack growth. An accurate representation of crack surfaces is essential when simulating problems in which the physics depend on the crack surface geometry. Some examples of these types of problems are hydraulically induced crack growth, crack growth with cohesive models and contact of crack surfaces due to crack closure.

Acknowledgments: The first two authors gratefully acknowledge the partial support of this work by the U.S. Air Force Research Laboratory Air Vehicles Directorate under contract number USAF-0060-50-0001. The support of the Computational Science and Engineering program at the University of Illinois at Urbana-Champaign is also gratefully acknowledged.

References

[1] J.A. Araújo and D. Nowell. The effect of rapidly varying contact stress fields on fretting fatigue. *International Journal of Fatigue*, 85:763–775, 2002. 20

[2] P.M.A. Areias and T. Belytschko. Analysis of three-dimensional crack initiation and propagation using the extended finite element method. *International Journal for Numerical Methods in Engineering*, 63:760–788, 2005. 2

[3] I. Babuška, U. Banerjee, and J.E. Osborn. Survey of meshless and generalized finite element methods: A unified approach. *Acta Numerica*, 12:1–125, May 2003. 4

[4] I. Babuška, G. Caloz, and J.E. Osborn. Special finite element methods for a class of second order elliptic problems with rough coefficients. *SIAM Journal on Numerical Analysis*, 31(4):945–981, 1994. 4

[5] I. Babuška and J.M. Melenk. The partition of unity finite element method. *International Journal for Numerical Methods in Engineering*, 40:727–758, 1997. 2, 4

[6] T. Belytschko, Y. Krongauz, D. Organ, and M. Fleming. Meshless methods: An overview and recent developments. *Computer Methods in Applied Mechanics and Engineering*, 139:3–47, 1996. 4

[7] S. Bordas and B. Moran. Enriched finite elements and level sets for damage tolerance assessment of complex structures. *Engineering Fracture Mechanics*, 73:1176–1201, 2006. http://dx.doi.org/10.1016/j.engfracmech.2006.01.006. 25

[8] B.J. Carter, P.A. Wawrzynek, and A.R. Ingraffea. Automated 3-D crack growth simulation. *International Journal for Numerical Methods in Engineering*, 47:229–253, 2000. 16, 28

[9] D.L. Chopp and N. Sukumar. Fatigue crack propagation of multiple coplanar cracks with the coupled extended finite element/fast marching method. *International Journal of Engineering Science*, 41:845–869, 2003. 2

[10] D.N. Dai, D.A. Hills, and D. Nowell. Modelling of growth of three-dimensional cracks by a continuous distribution of dislocation loops. *Computational Mechanics*, 19:538–544, 1997. 23

[11] D.N. dell'Erba and M.H. Aliabadi. Three-dimensional thermo-mechanical fatigue crack growth using BEM. *International Journal of Fatigue*, 22:261–273, 2000. 28

[12] Q. Duan, J.-H. Song, T. Menouillard, and T. Belytschko. Element-local level set method for three-dimensional dynamic crack growth. *International Journal for Numerical Methods in Engineering*, 2009. In press. http://dx.doi.org/10.1002/nme.2665. 2

[13] C.A. Duarte, I. Babuška, and J.T. Oden. Generalized finite element methods for three dimensional structural mechanics problems. *Computers and Structures*, 77:215–232, 2000. 4, 5, 6, 7

[14] C.A. Duarte, O.N. Hamzeh, T.J. Liszka, and W.W. Tworzydlo. A generalized finite element method for the simulation of three-dimensional dynamic crack propagation. *Computer Methods in Applied Mechanics and Engineering*, 190(15-17):2227–2262, 2001. http://dx.doi.org/10.1016/S0045-7825(00)00233-4. 2, 3, 6, 7

[15] C.A. Duarte, L.G. Reno, and A. Simone. A high-order generalized FEM for through-the-thickness branched cracks. *International Journal for Numerical Methods in Engineering*, 72(3):325–351, 2007. http://dx.doi.org/10.1002/nme.2012. 3, 6

[16] C.A.M. Duarte and J.T. Oden. An *hp* adaptive method using clouds. *Computer Methods in Applied Mechanics and Engineering*, 139:237–262, 1996. 4

[17] C.A.M. Duarte and J.T. Oden. *Hp* clouds – An *hp* meshless method. *Numerical Methods for Partial Differential Equations*, 12:673–705, 1996. 4

[18] M. Duflot. A study of the representation of cracks with level sets. *International Journal for Numerical Methods in Engineering*, 70:1261–1302, 2007. 2

[19] M. Duflot and S. Bordas. XFEM and mesh adaptation: A marriage of convenience. In *Eighth World Congress on Computational Mechanics*, Venice, Italy, July 2008. 7

[20] F. Erdogan and G.C. Sih. On the crack extension in plates under plane loading and transverse shear. *Journal of Basic Engineering*, 85:519–525, 1963. 14, 28

[21] FEACrack Version 2.7. Quest Reliability, LLC. Boulder, Colorado. http://www.srt-boulder.com/feacrack.htm. 1

[22] H. Gao and J.R. Rice. Somewhat circular tensile cracks. *International Journal of Fracture*, 33:155–174, 1987. 23

[23] T. C. Gasser and G.A. Holzapfel. 3D crack propagation in unreinforced concrete. A two-step algorithm for tracking 3D crack paths. *Computer Methods in Applied Mechanics and Engineering*, 195:5198–5219, 2006. 2

[24] T.C. Gasser and G.A. Holzapfel. Modeling 3D crack propagation in unreinforced concrete using PUFEM. *Computer Methods in Applied Mechanics and Engineering*, 194:2859–2896, 2005. 2

[25] W.H. Gerstle. *Finite and boundary element modelling of crack propagation in two and three dimensions using interactive computer graphics*. PhD thesis, Cornell University, New York, 1985. 28

[26] A. Gravouil, N. Moës, and T. Belytschko. Non-planar 3d crack growth by the extended finite element and level sets – Part II: Level set update. *International Journal for Numerical Methods in Engineering*, 53(11):2569–2586, 2002. 2, 8, 25, 28

[27] M. Griebel and M.A. Schweitzer, editors. *Meshfree Methods for Partial Differential Equations II*, volume 43 of *Lecture Notes in Computational Science and Engineering*. Springer, 2005. 4

[28] P. Jäger, P. Steinmann, and E. Kuhl. Modeling three-dimensional crack propagation – A comparison of crack path tracking strategies. *International Journal for Numerical Methods in Engineering*, 76:1328–1352, 2008. 2

[29] X. Jiao. Face offsetting: A unified framework for explicit moving interfaces. *Journal of Computational Physics*, 220(2):612–625, 2007. 3, 4, 8, 29

[30] X. Jiao, D. Wang, and H. Zha. Simple and effective variational optimization of surface and volume triangulations. *Engineering with Computers*, 2010. DOI: 10.1007/s00366-010-0180-z. To appear. 10

[31] D.-J. Kim, C.A. Duarte, and J.P. Pereira. Analysis of interacting cracks using the generalized finite element method with global-local enrichment functions. *Journal of Applied Mechanics*, 75(5):051107, 2008. 3

[32] D.-J. Kim, J.P. Pereira, and C.A. Duarte. Analysis of three-dimensional fracture mechanics problems: A two-scale approach using coarse generalized FEM meshes. *International Journal for Numerical Methods in Engineering*, 81(3):335–365, 2009. http://dx.doi.org/10.1002/nme.2690. 3

[33] P. Krysl and T. Belytschko. The element free Galerkin method for dynamic propagation of arbitrary 3-D cracks. *International Journal for Numerical Methods in Engineering*, 44:767–800, 1999. 3, 28

[34] Y.-S. Lai, A.B. Movchan, and G.J. Rodin. A study of quasi-circular cracks. *International Journal of Fracture*, 113:1–25, 2002. 23

[35] G.R. Liu. *Mesh Free Methods: Moving Beyond the Finite Element Method*. CRC Press, July 2002. 4

[36] W.K. Liu, Y. Chen, S. Jun, J.S. Chen, T. Belytschko, C. Pan, R.A. Uras, and C.T. Chang. Overview and applications of the reproducing kernel particle methods. *Archives in Computational Methods in Engineering: State of Art Reviews*, 3(1):3–80, 1996. 4

[37] U.M. Mayer, A. Gerstenberger, and W.A. Wall. Interface handling for three-dimensional higher-order XFEM-computations in fluid-structure interaction. *International Journal for Numerical Methods in Engineering*, 2009. In press. http://dx.doi.org/10.1002/nme.2600. 3

[38] J.M. Melenk and I. Babuška. The partition of unity finite element method: Basic theory and applications. *Computer Methods in Applied Mechanics and Engineering*, 139:289–314, 1996. 4

[39] N. Moës, A. Gravouil, and T. Belytschko. Non-planar 3D crack growth by the extended finite element and level sets – Part I: Mechanical model. *International Journal for Numerical Methods in Engineering*, 53(11):2549–2568, 2002. 2, 6

[40] NASGRO/FLAGRO. Fatigue crack growth computer program NASGRO/FLAGRO version 2.0. Structures and Mechanics Division, NASA/Lyndon B. Johnson Space Center, Houston, TX, 1992. 1

[41] J.T. Oden and C.A. Duarte. Chapter: Clouds, Cracks and FEM's. In B.D. Reddy, editor, *Recent Developments in Computational and Applied Mechanics*, pages 302–321, Barcelona, Spain, 1997. International Center for Numerical Methods in Engineering, CIMNE. http://citeseer.ist.psu.edu/17994.html. 7

[42] J.T. Oden, C.A. Duarte, and O.C. Zienkiewicz. A new cloud-based *hp* finite element method. *Computer Methods in Applied Mechanics and Engineering*, 153:117–126, 1998. 4, 5

[43] J.T. Oden and C.A.M. Duarte. Chapter: Solution of singular problems using *hp* clouds. In J.R. Whiteman, editor, *The Mathematics of Finite Elements and Applications – Highlights 1996*, pages 35–54, New York, NY, 1997. John Wiley & Sons. http://citeseer.ist.psu.edu/170015.html. 7

[44] H. Okada, H. Kawai, K. Araki, and T. Miyazaki. Three-dimensional crack propagation analysis based on VCCM (virtual crack closure-integral method) for tetrahedral finite element. *Advanced Materials Research*, 33-37:901–906, 2008. doi:10.4028/www.scientific.net/AMR.33-37.901. 28

[45] J. Oliver, A.E. Huespe, E. Samaniego, and E.W.V. Chaves. On strategies for tracking strong discontinuities in computational failure mechanics. In H.A. Mang, F.G. Rammerstorfer, and J. Eberhardsteiner, editors, *Fifth World Congress on Computational Mechanics*, Vienna, Austria, July 2002. 2

[46] J. Oliver, A.E. Huespe, E. Samaniego, and E.W.V. Chaves. Continuum approach to the numerical simulation of material failure in concrete. *International Journal for Numerical and Analytical Methods in Geomechanics*, 28(7–8):609–632, 2004. 2

[47] A. Paris and F. Erdogan. A critical analysis of crack propagation laws. *Journal of Basic Engineering*, 85:528–534, 1963. 14

[48] K. Park, J.P. Pereira, C.A. Duarte, and G.H. Paulino. Integration of singular enrichment functions in the generalized/extended finite element method for three-dimensional problems. *International Journal for Numerical Methods in Engineering*, 78(10):1220–1257, 2009. http://dx.doi.org/10.1002/nme.2530. 7

[49] J.P. Pereira and C.A. Duarte. Extraction of stress intensity factors from generalized finite element solutions. *Engineering Analysis with Boundary Elements*, 29:397–413, 2005. 15

[50] J.P. Pereira, C.A. Duarte, D. Guoy, and X. Jiao. *Hp*-Generalized FEM and crack surface representation for non-planar 3-D cracks. *International Journal for Numerical Methods in Engineering*, 77(5):601–633, 2009. http://dx.doi.org/10.1002/nme.2419. 3, 4, 6, 7, 8, 12, 15, 16, 25, 29, 30

[51] J.P. Pereira, C.A. Duarte, X. Jiao, and D. Guoy. Generalized finite element method enrichment functions for curved singularities in 3D fracture mechanics problems. *Computational Mechanics*, 44(1):73–92, 2009. http://dx.doi.org/10.1007/s00466-008-0356-1. 3, 4, 7, 8, 16

[52] L.P. Pook. Comments on fatigue crack growth under mixed modes I and III and pure mode III loading. In K.J. Miller and M.W. Brown, editors, *Multiaxial fatigue*, ASTM STP 853, pages 249–263, Philadelphia, 1985. American Society for Testing and Materials. 13, 28

[53] L.P. Pook. On fatigue crack paths. *International Journal of Fatigue*, 17(1):5–13, 1995. 28

[54] B. Prabel, A. Combescure, A. Gravouil, and S. Marie. Level set X-FEM non-matching meshes: Application to dynamic crack propagation in elastic-plastic media. *International Journal for Numerical Methods in Engineering*, 69:1553–1569, 2007. 3, 8

[55] M.A. Pustejovsky. Fatigue crack propagation in titanium under general in-plane loading — I: experiments. *Engineering Fracture Mechanics*, 11:9–15, 1979. 19, 20, 22

[56] J. Qian and A. Fatemi. Mixed mode fatigue crack growth: a literature survey. *Engineering Fracture Mechanics*, 55(6):969–990, 1996. 28

[57] T. Rabczuk, S. Bordas, and G. Zi. On three-dimensional modeling of crack growth using partition of unity methods. *Computers and Structures*, 2009. In press. http://dx.doi.org/10.1016/j.compstruc.2008.08.010. 2

[58] H.A. Richard, M. Fulland, and M. Sander. Theoretical crack path prediction. *Fatigue & Fracture of Engineering Materials & Structures*, 28:3–12, 2005. 13, 14, 15, 28

[59] R.J. Sanford. *Principles of fracture mechanics*. Prentice Hall, Upper Saddle River, NJ, USA, 2002. 1, 12

[60] J. Schijve. *Fatigue of structures and materials*. Kulver Academic, Boston, MA, USA, 2001. 1, 12

[61] M. Schöllmann, M. Fulland, and H.A. Richard. Development of a new software for adaptive crack growth simulations in 3-D structures. *Engineering Fracture Mechanics*, 70:249–268, 2003. 1, 14, 16

[62] M. Schöllmann, H.A. Richard, G. Kullmer, and M. Fulland. A new criterion for the prediction of crack development in multiaxially loaded structures. *International Journal of Fracture*, 117:129–141, 2002. 13, 15, 28

[63] J.A. Sethian. *Level Set Methods and Fast Marching Methods Evolving Interfaces in Computational Geometry, Fluid Mechanics, Computer Vision, and Materials Science*. Cambridge Monograph on Applied and Computational Mathematics. Cambridge University Press, 1999. 2, 8

[64] G.C. Sih and B.C.K. Cha. A fracture criterion for three-dimensional crack problems. *Engineering Fracture Mechanics*, 6:699–723, 1974. 13

[65] K. Sobczyk and B.F. Spencer. *Random Fatigue: From Data to Theory*. Academic Press, inc., San Diego, USA, 1992. 14

[66] T. Strouboulis, I. Babuška, and K. Copps. The design and analysis of the generalized finite element mehtod. *Computer Methods in Applied Mechanics and Engineering*, 81(1–3):43–69, 2000. 7

[67] T. Strouboulis, K. Copps, and I. Babuška. The generalized finite element method. *Computer Methods in Applied Mechanics and Engineering*, 190:4081–4193, 2001. 4

[68] N. Sukumar, D. Chopp, N. Moës, and T. Belytschko. Modeling holes and inclusions by level sets in the extended finite element method. *Computer Methods in Applied Mechanics and Engineering*, 190:6183–6200, 2001. 8

[69] N. Sukumar, D.L. Chopp, E. Béchet, and N. Moës. Three-dimensional non-planar crack growth by a coupled extended finite element and fast marching method. *International Journal for Numerical Methods in Engineering*, 76:727–748, 2008. 23, 25

[70] N. Sukumar, D.L. Chopp, and B. Moran. Extended finite element method and fast marching method for three-dimensional fatigue crack propagation. *Engineering Fracture Mechanics*, 70:29–48, 2003. 2

[71] N. Sukumar, N. Moës, B. Moran, and T. Belytschko. Extended finite element method for three-dimensional crack modelling. *International Journal for Numerical Methods in Engineering*, 48(11):1549–1570, 2000. 2, 6

[72] B. Szabo and I. Babuška. *Finite Element Analysis*. John Wiley and Sons, New York, 1991. 7, 15

[73] B. A. Szabo and I. Babuška. Computation of the amplitude of stress singular terms for cracks and reentrant corners. In T.A. Cruse, editor, *Fracture Mechanics: Nineteenth Symposium, ASTM STP 969*, pages 101–124, Southwest Research Institute, San Antonio, TX, 1988. 15

[74] H. Tada, P. Paris, and G. Irwin. *The Stress Analysis of Cracks Handbook*. ASME Press, New York, 3rd edition, 2000. 25

[75] R. Tian and G. Yagawa. Generalized nodes and high-performance elements. *International Journal for Numerical Methods in Engineering*, 64:2039–2071, 2005. 7

[76] R. Tian, G. Yagawa, and H. Terasaka. Linear dependence problems of partition of unity-based generalized fems. *Computer Methods in Applied Mechanics and Engineering*, 195:4768–4782, 2006. 7

[77] C. Timbrell, R. Chandwani, and G. Cook. State of the art in crack propagation. In *Journée Scientifique 2004: Les méthodes de dimensionnement en fatigue*, Fribourg, Switzerland, October 2004. Centre de Compétences Matériaux & Conception. 16

[78] A. Ural, G. Heber, P. Wawrzynek, A. Ingraffea, D. Lewicki, and J. Neto. Three-dimensional, parallel, finite element simulation of fatigue crack growth in a spiral bevel pinion gear. *Engineering Fracture Mechanics*, 72:1148–1170, 2005. 1

[79] P.A. Wawrzynek, L.F. Martha, and A.R. Ingraffea. A computational environment for the simulation of fracture processes in three-dimensions. In A. J. Rosakis, editor, *Analytical, Numerical and Experimental Aspects of Three Dimensional Fracture Process*, volume 91, pages 321–327, New York, 1988. ASME AMD, ASME. 1

[80] Zentech International Limited, http://www.zentech.co.uk/zencrack.htm. *ZENCRACK*, 2008. 1, 16